CONDUCTING FTO COATINGS PRODUCED USING ULTRASONIC SPRAY PYROLYSIS FOR HEATING APPLICATIONS

A THESIS SUBMITTED TO
THE GRADUATE SCHOOL OF NATURAL AND APPLIED SCIENCES
OF
MIDDLE EAST TECHNICAL UNIVERSITY

BY

BAŞAR SÜER

IN PARTIAL FULFILLMENT OF THE REQUIREMENTS
FOR
THE DEGREE OF MASTER OF SCIENCE
IN
METALLURGICAL AND MATERIALS ENGINEERING

SEPTEMBER 2018

Approval of the thesis:

CONDUCTING FTO COATINGS PRODUCED USING ULTRASONIC SPRAY PYROLYSIS FOR HEATING APPLICATIONS

submitted by **BAŞAR SÜER** in partial fulfillment of the requirements for the degree of **Master of Science in Metallurgical and Materials Engineering Department, Middle East Technical University** by,

Prof. Dr. Halil Kalıpçılar _____
Dean, Graduate School of **Natural and Applied Sciences**

Prof. Dr. Cemil Hakan Gür _____
Head of Department, **Metallurgical and Materials Eng., METU**

Prof. Dr. A. Macit Özenbaş _____
Supervisor, **Metallurgical and Materials Eng., METU**

Examining Committee Members:

Prof. Dr. Abdullah Öztürk _____
Metallurgical and Materials Engineering Dept., METU

Prof. Dr. A. Macit Özenbaş _____
Metallurgical and Materials Engineering Dept., METU

Prof. Dr. M. Kadri Aydınol _____
Metallurgical and Materials Engineering Dept., METU

Assist. Prof. Dr. Batur Ercan _____
Metallurgical and Materials Engineering Dept., METU

Assist. Prof. Dr. Erkan Konca _____
Metallurgical and Materials Engineering Dept., Atılım University

Date: 04.09.2018

I hereby declare that all information in this document has been obtained and presented in accordance with academic rules and ethical conduct. I also declare that, as required by these rules and conduct, I have fully cited and referenced all material and results that are not original to this work.

Name, Last name : Başar Süer

Signature :

ABSTRACT

CONDUCTING FTO COATINGS PRODUCED USING ULTRASONIC SPRAY PYROLYSIS FOR HEATING APPLICATIONS

Süer, Başar
M.S., Department of Metallurgical and Materials Engineering
Supervisor: Prof. Dr. A. Macit Özenbaş

September 2018, 93 pages

In this thesis, fluorine doped tin dioxide (FTO) coatings were deposited on AISI 304 stainless steel (SS) substrates using ultrasonic spray pyrolysis (USP) technique. Four different candidate insulating intermediate layers of TiO_2, MgO, Al_2O_3 and SiO_2 were selected and coated on AISI 304 using USP and investigated in order to overcome dielectric breakdown of FTO layer due to conductive nature of stainless steel substrate under the applied voltage. After the optimization of the process parameters for the depositions, only TiO_2 layer was successfully deposited while other oxides did not form continuous films on AISI-304 SS surface despite the efforts. SEM analysis, supported by back-scatter imaging, revealed thickness values of the layers for FTO and TiO_2, individually. Heating performances of the samples with various sheet resistance values were examined under various applied voltages. Heating experiments showed that 300 ^oC can be reached with 10 V of applied voltage without occurrence of an electrical breakdown of FTO coating having 160 nm thickness with TiO_2 intermediate layer of 660 nm. 28.6% efficiency of converting electrical energy into heat was calculated for thin FTO film while stainless steel showed only 7.3% efficiency. Also, cyclic heating experiments and humidity test indicated that FTO coatings are resistant against cyclic loadings and humid environment.

Keywords: fluorine doped tin dioxide, ultrasonic spray pyrolysis, heating applications, electrical breakdown, intermediate insulating layers.

ÖZ

ISITICI UYGULAMALARI İÇİN ULTRASONİK SPREY PİROLİZ YÖNTEMİYLE ÜRETİLEN İLETKEN FTO KAPLAMALAR

Süer, Başar
Yüksek Lisans, Metalurji ve Malzeme Mühendisliği
Tez Yöneticisi: Prof. Dr. A. Macit Özenbaş

Eylül 2018, 93 sayfa

Bu tez çalışmasında, flor katkılı kalay dioksit (FTO) tabakaları, ultrasonik sprey piroliz tekniği (USP) kullanılarak AISI 304 paslanmaz çelik altlıkların yüzeyleri üzerine kaplanmıştır. Çeliğin iletken olması sebebiyle FTO katmanının olası dielektrik çökümünün üstesinden gelmek için dört farklı aday yalıtkan ara katman belirlenmiş ve kaplanmıştır. Aday katmanlar TiO_2, MgO, Al_2O_3 ve SiO_2 olarak seçilmiş ve bu katmanlar arasından, sadece TiO_2 paslanmaz çelik üzerinde başarılı bir şekilde kaplanmıştır. TiO_2 katmanının gösterdiği yüksek kalite, homojen ve sürekli morfolojiyi diğer oksitler, belirlenen deney şartları altında gösterememiştir. TiO_2 ara katmanının belirlenmesinden sonra SEM analizi yapılarak, FTO ve TiO_2 katmanları için bireysel kalınlıklar tespit edilmiştir. Isıtma deneyi sonuçları, 660 nm kalınlığa sahip TiO_2 ara katman ile 160 nm kalınlığındaki FTO tabakasının elektriksel çöküme uğramadan 300 ^oC'ye 10 V ile ulaşılabildiğini göstermiştir. Uygulanan elektriksel enerjinin ısıya dönüşümü hususunda, yapılan deneyler ve verimlilik hesaplamaları çerçevesinde AISI 304 paslanmaz çeliğin verimliliği %7.3 iken, FTO kaplamaya sahip olan örneğin verimliliği %28.6 olarak bulunmuştur. Ayrıca, tekrarlı ısıtma deneyleri ve nem testi, FTO kaplamaların döngüsel yüklemelere ve nemli ortamlara karşı dirençli olduğunu kanıtlamıştır.

Anahtar Kelimeler: flor katkılı kalay dioksit, ultrasonik sprey piroliz, ısıtıcı uygulamaları, elektriksel çöküm, ara yalıtım katmanları.

To my family

ACKNOWLEDGEMENTS

I would like to express my deepest gratitude cordially to my supervisor Prof. Dr. A. Macit Özenbaş for his patience, motivation, guidance, advice, criticism, support and insight not only throughout this thesis but in many other studies.

It has been my pleasure and honor to work and share with my laboratory mates Kerem Çağatay İçli, Bahadır Can Kocaoğlu, Mustafa Burak Coşar, Emre Burak Yurdakul, Çağrı Özdilek, Hediye Merve Ertuğrul and colleagues Kıvanç Alkan, Bersu Baştuğ, Olgun Yılmaz. Also, I am very pleased for their brainstorming sessions, support and friendship during this study.

I am very grateful to Metallurgical and Materials Engineering Department, Middle East Technical University for all the support, especially on XRD and SEM analysis for this study.

I want express my gratitude to Mustafa Burak Coşar and ASELSAN for their help through Hall-Effect Measurements and Humidity tests.

I feel deeply grateful to the love of my life Dilan Vargün for her care, support, endless and selfless love during hard-working days.

Finally, many thanks go to my precious family for their caring, patience and support not only throughout this thesis but in whole my life with their never ending love.

TABLE OF CONTENTS

LIST OF TABLES

TABLES

LIST OF FIGURES

FIGURES

LIST OF ABBREVIATIONS

FTO	Fluorine doped Tin Dioxide
ITO	Tin doped Indium (III) Oxide
ATO	Aluminum doped Tin Dioxide
AZO	Aluminum doped Zinc Oxide
SEM	Scanning Electron Microscope
XRD	X-ray Diffraction
AFM	Atomic Force Microscopy
EDS	Energy-Dispersive X-ray Spectroscopy
TCO	Transparent Conducting Oxide
NSD	Nozzle to Substrate Distance
CVD	Chemical Vapor Deposition
PVD	Physical Vapor Deposition
USP	Ultrasonic Spray Pyrolysis
BDV	Breakdown Voltage
MSP	Magnetron Sputtering
SBP	Solution Based Process
PLD	Pulsed Laser Deposition
FEA	Finite Element Analysis
ECR-MOCVD	Electron Cyclotron Resonance - Metallic Organic Chemical Vapor Deposition

CHAPTER 1

INTRODUCTION

Renewable energy technology has received great attention from researchers and visionary entrepreneurs due to current global warming and pollution that has been with us over few decades. The urgent need have been risen to look out for special materials and methods that can be considered as an alternative for the old technology, which is now well accepted throughout the globe as the centre of environmental issues regarding global warming. Even though the non-renewable resources are getting scarce, there are few new and efficient resources to replace them, leading most of the researches to focus on efficient energy conversion. In order for a community to become CO_2 neutral, it is essential to minimize the unnecessary use of any kind of energy to decrease the consumption of both fossil fuels and other non-renewable energy sources that inevitably harm Mother Nature's breathing space [1].

Heating has always been a necessary utility for human kind from the early eras. We have been burning stuff ever since to generate heat to keep our houses warm. The resulting product of burning, CO_2, has already become a huge and unignorable issue that somehow needs to be kept under control. Even reducing the overall global waste, say about 1%, would tremendously help rejuvenation for the earth. Knowing the up-coming problems in the future, people around the globe have been advertising and creating smart and efficient designs that intend to help minimizing the waste energy.

Efficient designs and smart materials are holding the key for this subject. For heating applications, most of the industry is dominated by old-fashioned copper and steel wires and/or cylindrical resistors. These designs usually work under standard voltage supplied by the city, and attract huge amount of current which increases power consumption. Devices such as kettles and ovens used in our houses are mostly

designed to reach the desired temperature as quickly as possible. However, doing so highly increases the energy consumption and initiates the butterfly-effect of waste energy problem. In order to minimize this consumption, thin film heaters can be used. Also, conducting coatings on top of a substrate can result in a much more homogeneous temperature distribution. Commercial heaters even try to homogenize the temperature distribution putting a flat surface above the resistor itself and this causes a loss of heat simply due to air trapped in between both contacts, acting as an insulating layer. With conducting oxide coatings such problems would not exist. Another loss that occurs in commercial heaters is that the total mass of the resistor itself siphons the generated heat within itself. Using thin films heaters would require less of that energy for the upkeep. The desired temperature can be obtained with much less voltages across the heater simply thanks to having less mass to be heated up before-hand. There are several oxide materials which can be coated on a substrate using one of the many deposition techniques and can be used in heating applications.

Among the most popularly used conducting oxides, fluorine doped tin dioxide (FTO) shines among the others in terms of low material cost, high temperature stability and corrosion resistance. Combining these properties, films can be coated on a substrate to achieve a high-quality and homogeneous films. Most of the researches and applications for this matter focus on glass or silicon substrates while leaving any metallic substrates out-of-focus. Metallic substrates, like stainless steel, have several advantages over other brittle substrates like glass or silicon. Sudden temperature spikes during heating or cooling could cause problems for these substrates because of their brittle nature. Very thin layers that carry current result in a much more efficient approach to heating applications [2]. Also, deposition can be applied on sheet metals, like foils, which can be used in several special applications that require adjustable shaping, like a flexible heater [3].

The main concern of having a conductive oxide layer on a metallic substrate is the electrical breakdown phenomena. When an applied voltage exceeds the limit of the breakdown voltage value of the material under consideration, $V_{breakdown}$, it breaks down electrically and electrical current then starts to flow without much of a resistance. Since the thin films are generally around sub-micron level, it is logical to

assume that their breakdown voltage would be around several voltage per unit thickness in nm (V/nm). This unexpected electrical current flow occurs in nanoseconds and results in a sudden increase in the conductivity of the material. The reasons for this phenomena are generally caused by rapid destabilization of the trapped charges and governed by many property related events such as loading conditions, current density, thickness, temperature, porosity, microstructure, grain size and impurities [4]. In order to prevent this phenomena, it is essential to isolate the conducting film from the conductive substrate underneath. Introducing insulating layer sandwiched between the film and the metal surface is the ideal way of solving this problem. Having insulating intermediate layers, ability to work under higher applied voltages is expected.

The aim of this work is to generate heat efficiently through applied electrical voltage to the thin film deposited on stainless steel substrates. For this purpose, different intermediate layers of Al_2O_3, SiO_2, MgO and TiO_2 were deposited on AISI 304 stainless steel substrates and FTO layers deposited on top of each individual intermediate layers using ultrasonic spray pyrolysis method. After obtaining optimum process parameters such as temperature and nozzle-to-substrate distance, they were kept the same for the deposition of all layers. The experimental details are given in Chapter 3, extensively, after a literature survey. Results of the morphological characterizations and electrical properties of the samples were obtained using scanning electron microscopy (SEM), x-ray diffraction (XRD), energy-dispersive x-ray spectroscopy (EDS), atomic force microscopy (AFM), four-point probe measurements and they are presented in Chapter 4. The heating curves, breakdown behaviour, cyclic heating experiments, and humidity tests of the samples were discussed in chapter 4 and conclusions are given in Chapter 5.

CHAPTER 2

LITERATURE SURVEY

2.1 TRANSPARENT CONDUCTING OXIDES (TCOs)

Transparent conducting oxides (TCOs) have been attracting great attention and investigated by many researchers because of their superior properties to be used in various optoelectronic applications including thin film solar cells [5], flat panel displays [6], touch screens [7], organic light emission diodes (OLEDS) [8] and heating elements for defrosting/defogging window panels of vehicles [9], thick film gas sensors [10] and electro-chromic devices [10]. TCOs are preferred for these devices and applications due their sufficient electrical conductivity with a generous visible-light transparency. For LCD displays and other type of optoelectronic applications, it is a necessity to use a transparent electrode that is electrically conductive while showing transparent behavior. These materials have been researched, studied and produced over several decades, trying to reach the global needs. One of the best TCOs, which is tin doped indium oxide (ITO), is currently dominating the global market and is being practically used in many optoelectronic applications. Nowadays, researchers are leaning towards other TCOs than indium, which is a rare-earth metal, is getting scarce day by day. Many researchers are, therefore, focusing on solving these issues by replacing rare-earths with other candidate materials. Several TCOs are quite suitable for fully replacing ITO and these metals are much more abundant in the Earth's crust, compared to indium. TCOs that are widely researched and studied:

- Tin doped indium (III) oxide (In_2O_3:Sn, ITO)
- Aluminum doped zinc oxide (ZnO:Al, AZO)
- Antimony doped tin dioxide (SnO_2:Sb, ATO)
- Gallium doped zinc oxide (ZnO:Ga, GZO)

- Fluorine doped tin dioxide (SnO_2:F, FTO)

There are numerous deposition techniques for these oxides to be coated on different substrates. Generally, the chosen substrates for these coatings are glass or silicon, glass for optoelectronic applications and silicon for electronic applications. One of the most widely used deposition technique for ITO is magnetron sputtering (MSP) and this method is, in fact, in practical use for most optoelectronic applications. MSP method successfully delivers high-quality films to be used in the industry [11]. It delivers a high control over the thickness of the coating throughout the structure with a good precision. However, having such benefits comes with drawbacks. The major disadvantage of this method is that it requires a high-vacuum which prolongs the deposition time. It causes a problem considering an industrial mass production.

Generally, conducting oxide thin films are in poly-crystalline or amorphous forms that are grown on the substrate. The resistivity values for these coatings are in the order of 10^{-3} Ω.cm while holding a visible-light transmittance of 80-85% thanks to having a high band-gap energy. Combining both features of these properties, TCOs found a well-deserved front-line spot in optoelectronic industry [10].

TCO thin films have been extensively developed over the years, mostly towards n-type semiconductors rather than p-type, consisting of metal oxides. Even though there are many reports regarding p-type semiconductor coatings, they do not reach the criteria to be used as an electrode for heating applications [12]. It is well-known that the natural characteristics of the metal oxides like In_2O_3 or ZnO already show enough conductivity without any impurity doping. However, they are reported to be unstable at elevated temperatures making them impractical for heating applications. The conductivity of these materials are provided by the free electrons that exist within their microstructure either by oxygen donor and/or metal atom interstitial. There are many elemental dopants that have been researched and studied in order to increase certain properties of the conducting oxides, like Sb, F, Sn, Al, Ga, W, Ta, Y and Sc as well as compound dopants like $In_4Sn_3O_{12}$ and Zn_2SnO_4 [13]. The electrical properties of the doped metal oxide highly depend on the dopant type, precursors, deposition method and, of course, the deposition conditions. The reported electrical properties such as

resistivity, hall-mobility, carrier concentration, charge mobility and sheet resistance, therefore, show a great variance.

Since the substrates used in this work were AISI 304 stainless steels, considering optical properties (i.e. transparency) is rather unimportant. Looking at **Table 2.1**, one can observe variety of electrical conductivity values obtained in these films coated by different methods, ranging from 0.019 to 4762 $(\Omega.cm)^{-1}$. The range obtained in these works for carrier concentration is around in the order of 10^{20} cm^{-3} with thicknesses in sub-micron levels. Most of the substrates used in these studies, were glass. There were very limited amount of information in the literature regarding conducting oxide coatings on stainless steel substrates. Besides, those who conduct such researches generally focus on different material properties such as corrosion and contact resistances [14,15]. Since the oxides used in these coatings show high chemical stability, they can be used to enhance corrosion properties of the stainless steel surfaces especially when serious chemical attack conditions are under consideration.

The general idea of using conducting oxide is circling around the electrical properties provided from these coatings and enhancements in the desired surface properties. It is essential to understand the differences between these conducting oxides in terms of materials science aspect. After discussing some of the most commonly used conducting oxides in the up-coming sections, the comparison of the deposition techniques will be briefly explained.

Table 2.1 Table of several studies on different type of TCOs with variety of deposition methods given in terms of selected properties, where *NSD: nozzle-to-substrate distance, σ: conductivity, R_{sh}: Sheet resistance, Ø: Figure of merit, n: Carrier concentration, μ: Mobility, C.S.: Crystallite Size, %T: Transmittance of films, t: Film thickness, V: Solution volume, l: Mean free path, F.R.: flow rate.*

Ref.	Coating	Process	Substrate	σ $(\Omega.cm)^{-1}$	ρ (Ω.cm)	%T	R_{sh} (Ω/□)	Other(s)
[13]	SnO_2:Sb	Chemical Spray Pyrolysis	Glass	1449	$6.9x10^{-4}$	50-70%	4.21	E_{gap} = 3.5-3.97 eV, t = 0.8-1.64 μm μ = 19-25 $cm^2/(V.s)$
[16]	SnO_2:Sb	Spray Pyrolysis	Glass	820 - 1124	1.22- $0.89x10^{-3}$	~70%	8.84- 15.42	μ = 7.49-9.84 cm2/(V.s) n = 5.19-8.52x10^{20} cm^{-3}
[17]	SnO_2 & SnO_2:F	Chemical Spray Pyrolysis	PEI	-	-	~80%	-	t = 200 nm
[7]	SnO_2:Sb	R.F. Magnetron Sputtering	Quartz Glass	1215	$8.23x10^{-4}$	~86%	28	E_{gap} = 4.12-4.26 eV, t = 300 nm μ = 9.80 $cm^2/(V.s)$ n = 3.83x10^{20} cm^{-3}
[18]	SnO_2:Sb & SnO_2:F	Spray Pyrolysis	Glass	0.019 0.071	53.83 (FTO) 14.01 (ATO)	~88% ~87%	-	-
[19]	TiO_2	Electrophoretic Deposition	FTO, 304L, Titanium	-	-	-	-	-
[20]	SnO_2 & SnO_2:Sb	Spray Pyrolysis	Glass	389	$2.57x10^{-3}$	~90%	-	t = 450 nm, n = 3.67x10^{19} cm^{-3}

Table 2.1 (Continued)

[21]	SnO_2& SnO_2:F	Chemical Spray Pyrolysis	Glass	2632	$3.8x10^{-4}$	85.6%	3.42	t = 1112 nm, n = $2.49x10^{19}$ cm^{-3} μ = 6.59 $cm^2/(V.s)$, E_{gap} = 4.15 eV
[22]	SnO_2:F, SnO_2:Sb, SnO_2:In	Spray Pyrolysis	Borosilicate Glass	1000-4762	$1x10^{-3}$-$3.5x10^{-4}$	ATO: 80% ITO: 72%	15-20	t = 175-1380 nm
[10]	SnO_2:Sb	Spray Pyrolysis	Glass	-	-	-	-	-
[23]	SnO_2:Sb In_2O_3:Sn	Spin, Dip & Spray Coating	Borofloat Glass	-	$1.7x10^{-2}$ $3.4x10^{-3}$	~90%	250-1000	t = 400 nm
[24]	SnO_2:Sb	DC Magnetron Sputtering	Quartz Glass	1.82	$5.5x10^{-1}$	~80%	-	t = ~400 nm, n = $1.2x10^{19}$ cm^{-3} μ = 0.54 $cm^2/(V.s)$
[25]	SnO_2:Sb	Spray Pyrolysis	Glass & Quartz	1111.1	$9x10^{-4}$	~80%	28	n = $22x10^{19}$ cm^{-3}, μ = 32 V/(cm.s)
[26]	SnO_2:F & $GaSnO_2$:F	ECR-MOCVD	Stainless Steel 316	-	-	-	-	Contact ρ ($m\Omega.cm^2$): SS-316 = 279 FTO-coated-316 = 76 $ZnSnO_2$:F-coated-316 = 17

Table 2.1 (Continued)

[13]	SnO_2:F & In_2O_3:Sn	Spray Pyrolysis	Glass	1250-1667	~$8.0x10^{-4}$-~$6.0x10^{-4}$	~70-85%	-	n = $63x10^{19}$ cm^{-3}, n = $31.1x10^{19}$ cm^{-3} μ = 12.4 $cm^2/(V.s)$
[27]	SnO_2:F	Spray Pyrolysis	Glass	W_{FTO} M_{FTO} E_{FTO} P_{FTO}	$10.1x10^{-4}$ $12x10^{-4}$ $7.43x10^{-4}$ $5.08x10^{-4}$	73.4 72.4 63.8 87	11.5 5.02 5.38 3.71	N (P_{FTO}) = $21.2x10^{20}$ cm^{-3} μ (W_{FTO})= 38.58 $cm^2/(V.s)$
[28]	SnO_2:F	Spray Pyrolysis	Glass	-	8.82-$3.91x10^{-4}$	~75	20.4 4.2-5.3	t = 432-1071, n = $4.71x10^{20}$ cm^{-3} μ = 10.96 $cm^2/(V.s)$
[14]	SnO_2:F	ECR-MOCVD	SS-316	-	-	-	-	t = ~450 nm, Contact ρ:74 mΩ.cm^2 Corrosion resistance: 6.64 $\mu A/cm^2$
[29]	TiO_2	Sol-Gel, Dip-coating, Sputtering	SS	-	-	-	-	t = 250-350 nm
[26]	$ZnSnO_x$:F & SnO_x:F	ECR-MOCVD	SS-316	-	-	-	-	Contact ρ: 279, 76 and 35 mΩ.cm^2 for SS, FTO and FZTO
[30]	SnO_2:F	ECR-MOCVD	Glass	-	-	85%	26.85	t = ~1000 nm
[11]	SnO_2:F	Magnetron Sputtering	Glass		$6.71x10^{-3}$	83%	-	n = $1.46x10^{20}$ cm^{-3}, μ = 15cm^2/V.s E_{gap} = 3.80 eV

2.1.1 Fluorine doped tin dioxide (FTO)

Tin oxide (SnO) or tin dioxide (SnO_2) is a ceramic material that shows semiconducting behavior as well as other remaining transition metal oxides, hence has been investigated thoroughly by many researchers and being widely used in the optoelectronic industrial applications [31–33]. It shows a decent electrical conductivity in its intrinsic form which can be further improved by doping and it is considered as an oxygen-deficient n-type semiconductor. It exhibits different states for the oxygen as +2 and +4, which are named differently in the literature as stannous oxide for SnO and stannic oxide for SnO_2. SnO exists stably in litharge structure whereas SnO_2 shows tetragonal rutile structure. Several material properties of SnO_2 are given in **Table 2.2**. Sn^{+4} ions are located on the octahedral sites while O^{-2} ions remain on the trigonal planes of the tetragonal rutile structure, shown in **Figure 2.1**.

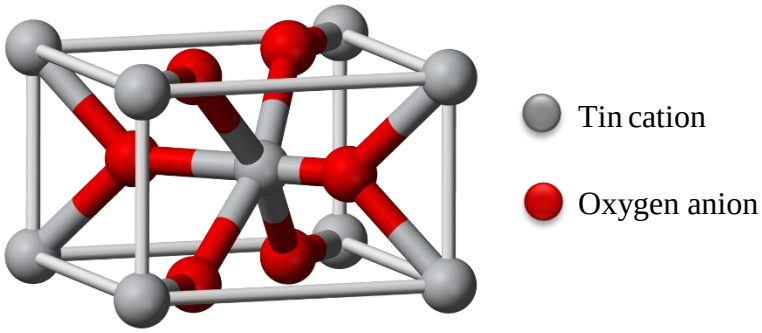

Figure 2.1 Crystal structure of SnO_2 which shows tetragonal rutile structure [34].

The lattice constants for the rutile structure are a = 0.4737 nm, c = 0.3185 nm with $\alpha = 90°$, $\beta = 90°$ and $\gamma = 90°$. The mineral of the SnO_2 was named as cassiterite, which is the main ore for tin and industrially can be reduced with carbon to obtain metallic tin, Sn [34].

Fluorine, F, is a common dopant element for SnO_2 which gives the name to fluorine-doped tin dioxide (FTO). Doping fluorine, a very reactive halogen, enhances the electrical properties of SnO_2 by simply replacing the oxygen ion within the crystal structure. Since the state of fluorine is -1 and replaces the oxygen that has -2, an extra electron is generated per each atom replaced. Introducing such impurities can be used

to achieve donor levels in the band gap. The extra electron generated through doping is donated to the conduction band of the material and hence it increases the electrical conductivity by increasing the carrier concentration [7]. Of course, there is a limit to this increase in the electrical conductivity simply due to the fact that there exists a solubility limit of tin dioxide for such impurities. One should realize that in order to replace oxygen ions with fluorine ions, they should have very close ion radii, in fact these radii are 0.117 nm and 0.122 nm, respectively. Therefore, it is possible to substitute these ions to generate higher number of charge carriers by introducing extra electron per substitution and obtain n-type semiconductor with further reduction of electrical resistivity [35].

Table 2.2 Some of the material properties of tin dioxide, SnO_2.

Material Property	**SnO_2**
Mineral name	Cassiterite
Molar mass (g/mol)	150.7
Density (g/cm^3)	6.95 at 20 ^oC
Solubility in water	None
Crystal structure	Tetragonal rutile, tP6
Melting point (^oC)	~1630
Boiling point (^oC)	~1900
Band gap (eV)	~3.6

Thanks to its wide band-gap, SnO_2 shows highly transparent behavior in the visible-light spectrum. However, as doping impurities increase, the electron concentration in the conduction band increases as well, while sacrificing a certain amount of transparency. Since the substrates used in this work were stainless steels, there is no need to consider any transparency-related topic. There are numerous amount of

deposition methods to introduce conducting oxide layers such as FTO. One of the most widely used technique is chemical vapor deposition (CVD) which is quite expensive [36]. Despite its cost, this technique generally yields a high-quality and homogeneous films across the substrate surface. Spray pyrolysis is another deposition method to achieve homogeneous films, using spray solutions that include precursors of tin dissolved either in water or in alcoholic solvents accompanied with the precursors of the dopant element. Altering the process parameters such as temperature, solution volume and molarity, different properties (thickness, sheet resistance etc.) of the FTO layers can be achieved. By optimizing the process parameters, the resulting properties of the FTO layers are quite close to the ones that were deposited by expensive techniques.

2.1.2 Tin doped indium (III) oxide (ITO)

Indium (III) oxide (In_2O_3) is the most widely used TCO in the industry due to its remarkable electrical and optical properties. Well deposited ITO films show more than 90% transparency in visible-light region with a sheet resistance value less than 10 Ω/□. Due to this combination of optical and electrical properties, ITO films are mostly preferred in the industry. However, due to scarcity of indium, which is the main element for ITO, and its vulnerability against high temperature create a problem, especially when heating applications are under consideration. Some of the material properties of indium (III) oxide are given in **Table 2.3**.

There exists two different crystal structures for the crystalline indium (III) oxide, cubic and rhombohedral, a high-temperature phase. Doping impurities like tin, further improves the electrical properties of the oxide. Recently, in order to increase the infra-red transmittance of In_2O_3, several studies have been conducted with hydrogen doping into In_2O_3 structure using radio-frequency magnetron sputtering (RF magnetron sputtering) technique with subsequent heat treatment to conserve the electrical properties of the film [37]. Besides RF magnetron sputtering, there are many other production techniques that have been studied throughout the years such as spray pyrolysis, electron-beam evaporation and sputtering.

Table 2.3 Some of the material properties of indium (III) oxide, In_2O_3.

Material Property	**In_2O_3**
Molar mass (g/mol)	277.7
Density (g/cm^3)	7.18 at 25 ^oC
Solubility in water	None
Crystal structure	Cubic, cl80
Melting point (^oC)	~1900
Band gap (eV)	~3

2.1.3 Antimony doped tin dioxide (ATO)

Tin dioxide, SnO_2, was already explained in chapter 2.1.1, regarding electrical and optical properties. When the dopant is antimony, Sb, the resulting structure is then called antimony doped tin dioxide (ATO). Comparable with FTO, ATO also has good electrical conductivity and transparency. It mostly finds a spot for itself in the energy storage devices such as lithium-ion batteries as anode. Also, with the help of screen-printing, it is possible to mass produce with much thicker films. Generally, the precursors used to obtain ATO films are chlorides, like $SbCl_3$ or $SbCl_5$ for the antimony doping [38].

2.1.4 Aluminum doped zinc oxide (AZO)

Zinc oxide, ZnO, is also another wide band gap semi-conductor that its electrical properties can further be improved by doping impurities, showing n-type behavior. It shares most of the application areas with the other conducting oxides like liquid-crystal displays (LCD), light-emitting diodes (LED) and transparent heaters [39]. The properties of AZO films make it very appropriate to be used on flexible materials for electronic purposes [40]. Some of the substrates used for AZO coatings are glass,

polyethylene terephthalate (PET), polyethylene naphthalate (PEN) and several other plastic materials. Magnetron sputtering is a costly but a high-quality coating technique that is used for AZO. The crystal structure that is the most stable under normal conditions is hexagonal wurtzite structure. The unstable phase of the zinc oxide exhibits cubic zincblende structure. The lattice constants are a = 0.32 nm and c = 0.52 nm for the hexagonal structure with c/a ratio as 1.625, which is highly close to the theoretical c/a ratio (1.633) for the hexagonal structure [41]. The properties of zinc oxide, ZnO, are slightly distinct from tin dioxide, SnO_2, as given in **Table 2.4** The mineral itself, named as zincite, is commercially used in many areas such as production of glasses, several ceramics, rubbers and paints.

Table 2.4 Some of the material properties of zinc oxide, ZnO

Material Property	**ZnO**
Mineral name	Zincite
Molar mass (g/mol)	81.4
Density (g/cm^3)	5.6
Solubility in water	Negligible
Crystal structure	Hexagonal Wurtzite
Melting point (^oC)	~1980
Band gap (eV)	~3.3

2.2 PRODUCTION TECHNIQUES

Over few decades, there have been many studies regarding thin film deposition techniques, several new-techniques have been introduced to the literature that require further research. Improved film homogeneity, quality and suitability to a certain process can be achieved through optimization of the process parameters. These methods are generally categorized into three major groups: Physical Vapor Deposition

(PVD), Chemical Vapor Deposition (CVD) and Solution Based Processes (SBP). There are several different production techniques under each category and each one has different process conditions and parameters [42–44]. Their classification is done by simply considering their type of process involved within, either physical or chemical. Even some of these techniques have several sub-classifications, however, these and some of the methods given in **Table 2.5** will not be discussed in this work whereas ultrasonic spray pyrolysis will be considered.

Table 2.5 Some of the deposition methods that are studied, researched and/or used in the industrial applications.

Deposition Methods		
Physical Vapor Deposition (PVD)	**Chemical Vapor Deposition (CVD)**	**Solution Based Processes (SBP)**
Thermal evaporation	Metal-organic CVD	Spin coating
Sputtering	Plasma enhanced CVD	Dip coating
Pulsed laser deposition	Low pressure CVD	Spray pyrolysis
Molecular beam epitaxy	Atmospheric pressure CVD	

In the CVD techniques, generally a gaseous phase is involved in the deposition. When PVD is considered, the methods such as thermal evaporation, sputtering (direct-current, DC and radio-frequency, RF), pulsed laser deposition (PLD) and molecular beam epitaxy exist within the scope of the deposition methods. SBP, as the name implies, involves a solution of the desired material for the coating to be deposited onto the substrate surface. These methods include spin coating, dip coating and spray pyrolysis. There are several other deposition methods which are not included in **Table 2.5** such as electron beam evaporation and atomic layer deposition.

2.2.1 Solution Based Processes

2.2.1.1 Ultrasonic Spray Pyrolysis

Ultrasonic spray pyrolysis (USP) is one of the deposition methods used to coat thin films on the substrate using a spray solution. One of the first spray pyrolysis experiment, CdS coating, was done by Chamberlin and Skarman [45]. Ever since there have been a lot of studies with USP method not only regarding research but also in its industrial usage. USP is a suitable deposition technique that can be used in producing large scale products as well as for mass production. There are several major advantages of this method that suppress other production techniques such as its ease of parameter control, high-flexibility for the process parameters, low-cost, ability to achieve high-quality films. Combining all these benefits with no-vacuum-requirement, yields a low-cost, effective and efficient process to be used both in film deposition industry and related researches. Due to above-mentioned simplicities of this method, it is possible to achieve high productivity on large scales for the formation of various thin films: metal oxides, chalcogenides and superconducting materials [46].

A schematic representation of a USP system is given in **Figure 2.2**. In a typical USP process, a precursor solution (or spray solution) is prepared having the desired materials dissolved in the solution. The mist from this solution is generated and carried onto the substrate. The droplets carried are generally in very small size and contain desired materials. These droplets, then, are blown onto the substrate which is generally pre-heated. The key point here is that the chemicals selected for the spray solution must be volatile at the temperature of the substrate so that the remaining products of the reaction would remain on the substrate and form a film [47].

When the process conditions are considered, spray pyrolysis offers numerous advantages. It is quite easy to introduce almost any desired element by simply adding it into the spray solution. The doping amount can also be altered by simply changing the proportion of the dopant in the spray solution. Spray pyrolysis does not require any vacuum compared to most of the CVD systems like sputtering which gives a huge promotion for the large scale and mass production. The deposition rate, which also controls the thickness and growth of the film on the substrate, can be controlled

with ease by controlling the process parameters such as temperature, spray rate and molarity of the spray solution. Since the temperature range required for this method can be considered as medium temperatures (room temperature-to-700 ^{o}C), there will not be any temperature-related problems for the substrate as long as the substrate can withstand the process temperature. Also, working at low temperatures makes it possible to coat polymeric, synthetic or organic materials that cannot withstand elevated temperatures.

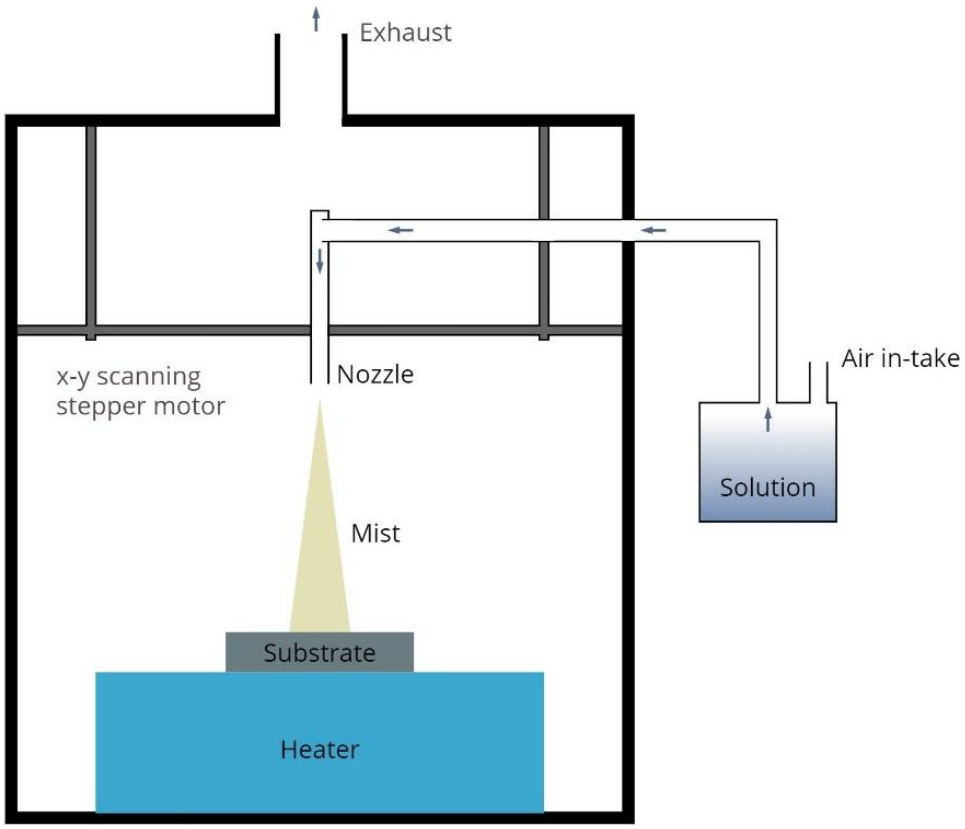

Figure 2.2 Schematic drawing of ultrasonic spray pyrolysis (USP) system used in this work.

The major components of the USP system are a solution chamber, air-in-take, a hose to carry the mist, spray nozzle, ultrasonic nebulizer, exhaust, thermocouple and a heater. There may be several alterations with these components which result in a different technique. Over the years researches showed that these alterations can be used just like any other deposition method with slight variations. Some of these methods are: corona spray pyrolysis in which the droplets enter a corona discharge

and transported via an electric field to the substrate and electro-static spray pyrolysis where the mist is generated by an electrohydrodynamic force. However, since these methods are out of the scope of this work, no further explanation will be given.

In some of the production methods for thin films which require quite a large amount of power like magnetron sputtering, generally local-heating of the substrate is a problem. The sudden temperature change in a specific portion of the substrate material can alter the morphology and the properties of the substrate material as well as alteration of the temperature can also be problematic for the coating itself. Lastly, since the spray solution is easily fed into the spraying system, it is possible to change the composition of the solution during the process. Following such routes, one can obtain multi-layered films and/or films with compositional gradients [47]. Some previously conducted studies with different coatings are summarized in **Table 2.6**.

Table 2.6 Some of the previously studied thin film materials deposited by USP.

Coated material	Precursors	Substrate	References
SnO_2	$SnCl_4$	Glass	[44]
SnO_2:F	$SnCl_4$, NH_4F	Glass	[42]
WO_3	$W(CO)_6$	Silicon wafer	[48]
Al_2O_3:Tb	$AlCl_3$, $TbCl_3$	Glass	[43]
Co_3O_4	$CoCl_2$	Glass	[49]
$LiCoO_2$	$LiAc.2H_2O$, $Co(NO_3)_2$	Stainless steel	[50]
CdTe	$CdCl_2$, TeO_2	Glass	[51]
$YBa_2Cu_4O_8$:$AgNO_3$	$Y_2(NO_3)_2$, $Ba(NO_3)$ $Cu(NO_3)_2$, $AgNO_3$	MgO	[52]

It is essential to generate uniform droplet size in order to obtain homogeneous films across the substrate. By vaporizing the spray solution it is possible to obtain sub-

micron sized droplets. When the generated mist meets the substrate that is pre-heated, the solvent evaporates and the film forms. Therefore, solvent and solute selection are essential in this matter since it will affect the wetting-condition. Versatility of this method enables numerous films to be deposited on a substrate.

2.2.1.2 Spin Coating

Spin coating is another technique that consists of an adjustable spinner that spins the substrate with a certain speed which spreads the small amount of solution applied onto the substrate, as seen from **Figure 2.3**. With the help of centrifugal force which causes the rotational-motion, the solution is dispersed with a high uniformity across the substrate surface. The evaporation of the solvent above the substrate leaves the desired film material on the surface. The key point of this method is to control the process parameters such as the viscosity, concentration of the solution, spin steps, temperature, spin speed and acceleration. Even though there exist several challenges need to be overcome, it offers a variety of coatings that can be applied on various sizes of substrates. It is possible to coat very small substrates (mm^2) or large substrates (m^2). Generally the applied coatings are metal oxides and TCOs. The drawbacks of the spin coating technique are that it requires a flat surface and during spin coating process and most of the solution is wasted due to the centrifugal force. Even though it is not a problem for research purposes, having more than 80% waste solution might be a problem considering mass production of manufacturing [36,53,54].

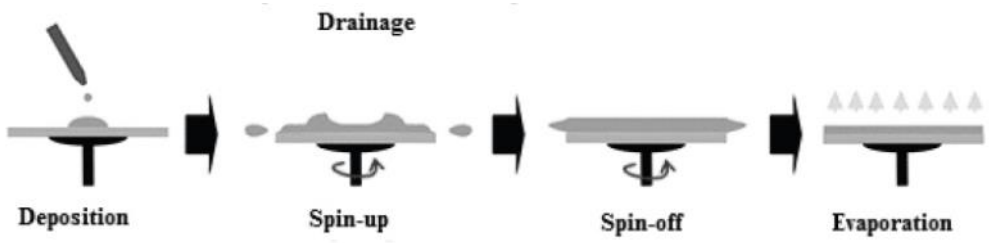

Figure 2.3 Schematic representation of spin-coating process [36].

2.2.1.3 Dip Coating

Dip coating have already found itself a well-deserved spot in the coating industry due to its ability to be continuously deposited and to be applied on large-scale substrates. Dip coating also requires a solution in which the substrate is immersed for a certain amount of time and then taken out, as shown in **Figure 2.4**.

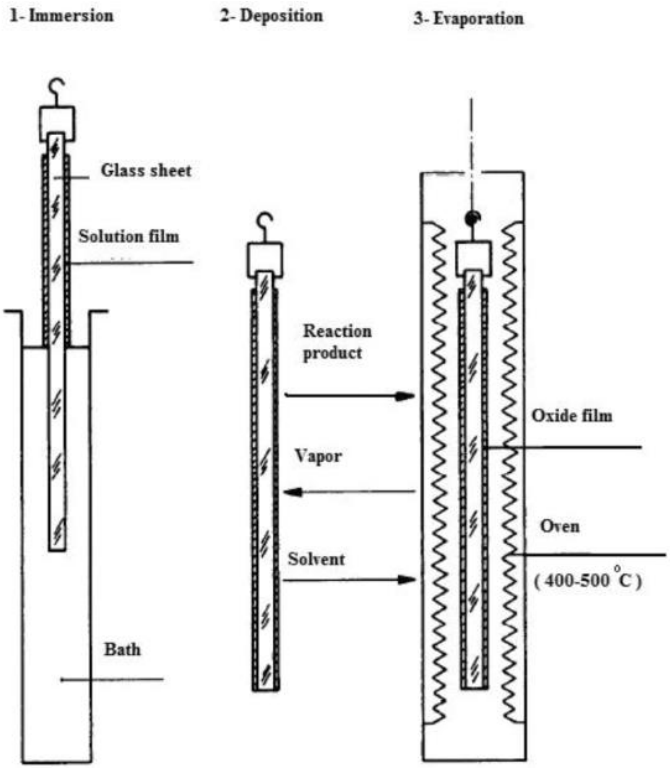

Figure 2.4 Schematic representation of dip-coating process [36].

The thickness of the deposited film is controlled by the solution concentration, immersion time, viscosity of the solution and withdrawal-speed. Also, variation of the film thickness can be achieved by introducing an angle during withdrawal. During withdrawal the excess solution is drained from the substrate leaving a thin layer of the solution above the surface. Subsequent evaporation, or a heat treatment for the remaining precursor solution may be required in order to evaporate any excess solvent or residual organic molecules [54].

One of the major drawbacks of this method is that coated material generally can easily be peeled off. This is simply due to the weak adhesion of the coating onto the substrate.

Also, since the film deposited onto the surface tends to go through volumetric shrinkage during drying step, a crack can be introduced inside the deposited film due to the residual stresses employed within. Despite these drawbacks, due to above-mentioned advantages, it is often used in industrial coating production.

2.2.2 Physical Vapor Deposition

2.2.2.1 Sputtering

Sputtering technique is often used to deposit thin films both in industry and researches. The deposition occurs in a vacuum chamber to avoid any inhomogeneity, low-quality coating. After a high amount of vacuum is applied to the chamber, the chamber is then filled with a process gas, depending on the coating type, which can be oxygen, O_2, Argon, Ar or nitrogen, N_2. After filling is completed, power is fed into the system in order to obtain plasma state inside the chamber. The energy source chosen for the system actually defines the type of sputtering system such as: radio-frequency (RF) and direct-current (DC). The electrical energy given to the gaseous phase inside the chamber, accelerates the electrons and forces them to move from cathode to anode, as shown in **Figure 2.5**. These electrons interact with the gas filled inside the chamber and pulls off the electron from the gas atoms, ionizing them (e.g. Ar^+). The pre-placed target material, which is the material source for the coating, is bombarded with these high-kinetic energy ions which have high enough energy to snatch atoms away from the surface of the target. The substrate that is desired to be coated with the target material is placed along the path is then starts to collect all the atoms that are split. The process is continued until a desired coating thickness is achieved [55,56].

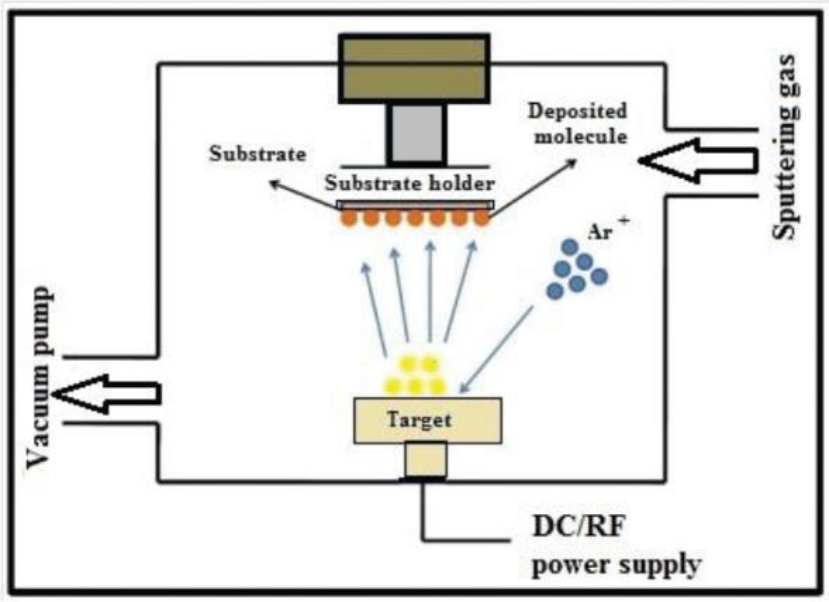

Figure 2.5 Schematic representation of a sputtering system [36].

The bombardment of the substrate can cause over-heating if the process is not well-controlled and this may cause damage to its structure. Besides, the deposition rate is quite low compared to other coating techniques. There have been improvements for this method both to increase the deposition rate and also to reduce the possibility of structural damage through over-heating of the substrate. Also using magnetrons yields a strong magnetic fields to constrain charged particles in the vicinity of the target material, increasing the collisions happening [55]. There are several sputtering techniques that uses different methods for the deposition such as ion-beam sputtering, reactive sputtering, RF-DC magnetron sputtering and ion-assisted sputtering [36].

2.2.2.2 Pulsed Laser Deposition

Pulsed laser deposition (PLD) method is categorized under PVD techniques in which a high-power laser beam is employed onto the target material. The material is vaporized due to introduced energy with focused beam, as shown in **Figure 2.6**. The mechanism and process requirements used in PLD is similar to the sputtering. The detached material due to high- energy introduced deposits on a pre-determined substrate and forms a film. The process requires high vacuum or a process gas like

oxygen, O_2, which is used to oxidize the deposited films or argon, Ar. Even though the schematic view and brief explanation of the process seem easy and simple, the kinetics behind the process is highly complex [36,57,58].

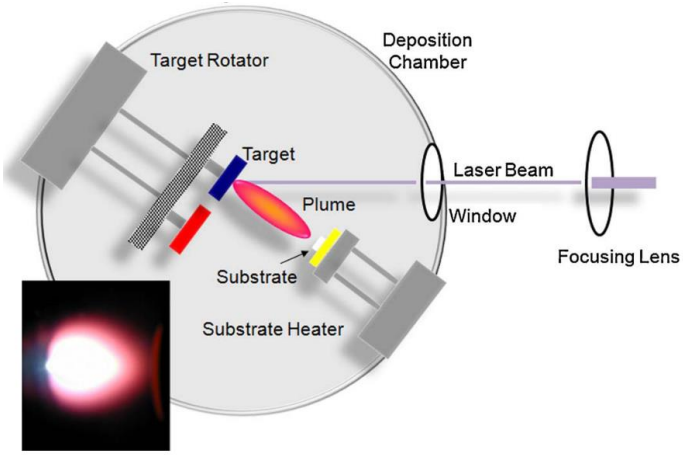

Figure 2.6 Schematic representation of pulsed-laser deposition process with inset showing actual photograph of the plume during processing [57].

The process parameters that determines the quality of the deposited films are the process temperature, laser power, target material quality, substrate surface quality, chamber pressure (especially for coatings which require oxygenation) and target-to-substrate distance. One of the major advantages of PLD is that it is possible to obtain a pre-defined compounds with complex stoichiometry. Conducting oxides and metallic layers can easily be obtained using PLD. Just like sputtering method, the requirement for a high-vacuum is the major drawback of this deposition technique. Also, the energetic particles ejected from target surface may collide with the substrate surface, deteriorating the surface quality of the film via forming defects. Despite these disadvantages, PLD offers a potential application areas for sensors, optoelectronics and bio-medicine, especially for representative prototypes [57].

2.2.3 Chemical Vapor Deposition

2.2.3.1 Plasma Enhanced Chemical Vapor Deposition

Plasma enhanced chemical vapor deposition (PE-CVD) is based on depositing thin films on a solid substrate using gaseous (vapor) state of the desired coating material. The chemical reactions occur during the process between the gases and reactions are caused by the plasma that is created in the chamber. The plasma is generated inside the chamber by using different ways such as either by alternating current (AC) or by direct current (DC). The chamber is filled with the reacting gases so that the discharge between the electrodes would take place. There are several essential process parameters for this technique such as chamber pressure, frequency, voltage and distance between the electrodes. The conductivity of the materials used also carries an important aspect since discharges can be generated easier even at low pressures. The films produced by PE-CVD generally show good quality and dense structure. Even though the deposition rate of the method is faster than other high-quality-deliver techniques (sputtering, thermal evaporation etc.), unfortunately the film uniformity is generally worse. The selection of the precursor combined with the gases is quite important to obtain the desired material. Several examples of PE-CVD coated films are: amorphous-SiGe:H and metal nitrides (MN_x where M = Fe, Co, Ni, Cu, Zr, Hf, Ta, Cr, Ta and W) [59,60].

2.3 ELECTRICAL HEATING

Over the years, in order to satisfy the needs for heating, electrical sources have been used. Conventional solutions for heating are generally based on coiled and wired designs. There are numerous applications using these coils and wires to convert electrical heat that is supplied either directly by the electrical power plants or from battery-like devices. Generally, the size or the cross-section area of these coils and wires determine the current flow through the material which results in desired temperature to be reached due to Joule Heating effect. The concept of this effect in an

integrated circuit is schematically shown in **Figure 2.7** and further explanation will be given in section 2.3.1.

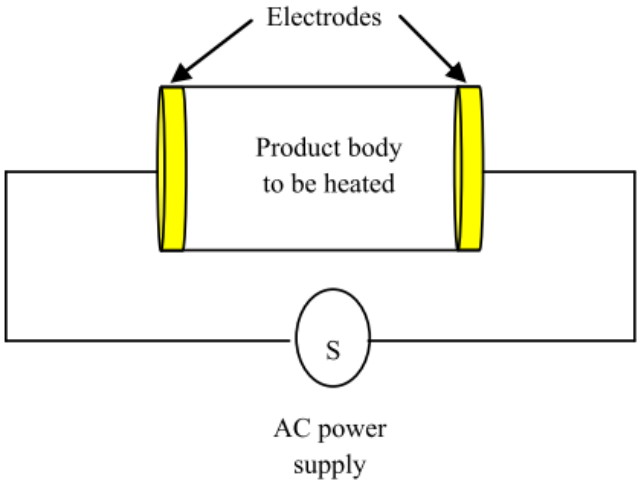

Figure 2.7 Schematic drawing showing the ohmic heating principle [2].

Electrical heaters are mostly used in our everyday lives such as ovens, irons, kettles, toasters and cookers. Heater surfaces are also available for scientific purposes. All these devices used in different areas and purposes show different designs in order to satisfy the specific desire for heating. The most important concern in these designs is to distribute the temperature evenly over the surface to obtain highest efficiency possible. The coiled or wired designs usually fail in terms of temperature distribution. In these designs, there exists a temperature gradient where some part of the system reaches a higher temperature. Also, the trapped air in between the coils or wires drastically decreases the heat flow since air behaves as almost like an insulating gaseous medium. Another problem here is that the coils and wires should be separated from the material that is considered to be heated. The gap in between these parts also decreases the efficiency of the heating device. Even though there is a great effort to get better temperature distribution, it is theoretically inevitable. These design are still widely used due to its low-cost manufacturing, low-material costs and ease of mass production. Also, produced wires or coils can easily be integrated and connected to the electrical circuit disregarding the efficiency of the device.

Apart from conventional heaters, recently a new window has opened which is considered as a much more efficient way of heating. Thin film heaters are a hot-topic research due to their ability to deliver heating with a much higher efficiencies while the mechanism of the heat release is very similar compared to conventional heaters. The difference in both designs, in terms of temperature distribution, have been proven by both experimental and simulation methods using finite element thermal analysis (FEA) by many researchers [61].

It is rather easy but essential to use FEA in order to obtain the best geometric design for an application that would maximize the potential heat output. Inputting the material properties such as electrical conductivity, film thickness, dimensions, emissivity, applied voltage, current flow and ambient temperature, one can easily find out the saturation temperature of the design with these given parameters. Experimental studies have shown that these simulations are in agreement with the experimental results within an acceptable deviation. Mostly, the experimental methods either use thermal cameras, infra-red cameras or thermocouples to measure the temperature. Even though the high-cost of the equipment, with the help of technological improvements in the thermal camera systems, it is possible to observe overall temperature distribution throughout the surface with high precision. Another advantage of using simulations is that, repetitive heating can be studied, without spending work and time for heating and cooling of the heaters with experimental work, in order to understand the behavior of the materials under thermal cycling conditions. This is rather important, especially for the thin film heaters, since the mismatch of thermal expansion coefficients between the substrate and the thin film material would be inevitable and may become the major potential problem considering excessive number of heating cycles [42,43,48,62,63].

2.3.1 Joule Heating Effect

The heat release during the passage of electrical current through a conductor is simply called Joule Heating Effect. This effect is contributed to the scientific community by James Prescott Joule during his studies regarding heat which eventually led to the 1st law of thermodynamics which explains the conservation of energy. He came up with

a well-known formula that explains the relationship between the resistor (R) and the current (I), also stating that this current flow results in a heat dissipation from the conductor. This effect is also called “ohmic heating” or “resistive heating”.

$$V = IR \qquad \text{Eq. [2.1]}$$

$$P = IV = I^2R \qquad \text{Eq. [2.2]}$$

The simple relationship between these components are more than enough to explain the behavior of the materials under an applied voltage (V) giving numerical information about the power (P) generated in terms of *joule per second*, J/s or *watt*, W. The energy output that is delivered from the system during *time*, t, is also used to understand the power – energy relationships using the equation:

$$E = Pt = I^2Rt \qquad \text{Eq. [2.3]}$$

which yields the energy output in terms of j*oule*, *J*. As simple as the equation is, it does not express that the energy output can be maximized by obtaining maximum current flow possible. There must exist some sort of resistance within the material in order to generate heat. The scattering events and collisions occurring during the current flow constructs the main contribution to the heat dissipation [2,64]. The heat evolved can be calculated from the equation:

$$Q = mC_p(T_{final} - T_{initial}) \qquad \text{Eq. [2.4]}$$

The performance and the efficiency of the heating system can be calculated from the following equation in which the efficiency can be calculated by using:

$$Efficiency = \frac{Energy\ required\ for\ heat}{Total\ Energy\ Input} = \frac{mC_p(T_f - T_i)}{\sum VI\Delta t} \qquad \text{Eq. [2.5]}$$

2.3.2 Heating Applications

There have been numerous applications that have been developed ever since the potential of conversion of electrical energy into heat was discovered. Innovators and

researchers are still focusing of improving the efficiencies of these devices to reduce the cost. Common applications using the principles of electrical heating are available both in households and as well as industrial or laboratory processes.

Different designs, materials, power amounts and objectives are used in these devices such as kettles, ovens, electrical heaters (radiant, fan etc.), irons, heating-plates, furnaces etc. A representative design for both examples is given in **Figure 2.8**. Besides commercially used heaters, industrial heaters are available with high precision, large heating area and quick-temperature-response. When large amounts of power is needed for a specific high-temperature process, mostly electrical infrastructure is used. The main drawback regarding this matter is that most of the electrical power is not effectively transferred into heat, thus resulting in a quite ineffective and inefficient way of heating. Rather than increasing the effectiveness of the energy transfer mechanism, generally the design of the structure is optimized to reduce heat-loss to the surroundings via introducing insulating materials that cover entire outer surface.

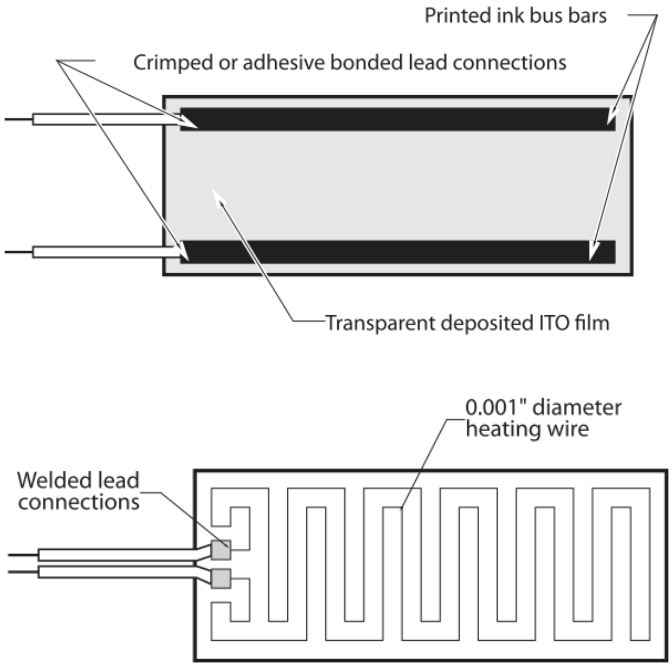

Figure 2.8 Comparison of hypothetical designs of (above) thin film heater and (below) wire-wound heater [61].

The thin film heaters are quite suitable for low-to-medium temperature applications since either film or the substrate materials tend to degrade, decompose or have microstructural alterations at elevated temperatures. Having higher efficiencies compared to commercial wire-wound designs, enable thin film heaters as a viable replacement to lower the energy consumption. Also, when oxide conductors are considered, due to their nature of resistance against chemical attacks and being thermally and chemically stable, these oxide conductors can take part in conditions in which harsh chemical environment exists while commercial steel or copper wires would be practically not possible to be used as heating elements [61].

2.4 DIELECTRIC BREAKDOWN

Dielectric breakdown (or electrical breakdown) phenomena is basically when an unexpected amount of current flow occurs through the material when an applied voltage exceeds the electrical breakdown limit of the material. This phenomena results in a partial electrically conductive material when its breakdown strength is reached and current starts to flow without any resistance. A naturally occurring example for this concept is thunderbolt, as given in **Figure 2.9**.

Figure 2.9 Photograph of lightning striking the ground [66].

The limit of the material that can withstand the maximum voltage without electrically breaking down is named in the literature as "*breakdown voltage*" (BDV), with a unit of volts per distance, V/nm [65]. This phenomenon is especially important for insulating materials used in the electrical devices in order to separate conducting parts. Exceeding the limit of the insulating part would result in a short circuit. There are many studies that explains electrical breakdown both theoretically and experimentally. The mechanism, basically, is that when sufficiently high electrical field is applied, the electrons are forced to move from valence band to the conduction band. When the predefined E_{gap}, which is the band gap of the material that simply separates the bands, is overcome, electrons create a path for the current flow.

As many other material properties are, the breakdown behavior of a material is also dependent on many things such as temperature, microstructure, loading conditions, thickness, geometry, porosity, grain size, impurities, number of charge carriers and charge mobility. The temperature dependence can easily be explained by the fact that electrons become much easier to excite to conduction band with increasing temperature, which eventually affects the breakdown strength of the material. When the heat dissipation from the material is larger than the heat input, the temperature lowers. The atomic vibrations, number of vacancies and charge mobility are all dependent on temperature which needs to be considered for breakdown strength [67]. Grain boundaries, although not directly, are also a key factor for the determination of the breakdown strength of the material. The main contribution is delivered by the increase in pore fraction and pore size correlated with grain size just like the inhomogeneous impurity content in the vicinity of the grain boundaries which can alter the breakdown strength. Also, the interaction of the individual atoms along the boundary are quite different than the ones inside the grains due to mismatches and missing bonds because of the open structure. The grain boundaries provide a potential route for the electrons to be transported under an applied voltage. Increasing the grain boundary area (i.e. decreasing the grain size) would make the material likely to form a network for the electrical conduction, which eases and favors electrical breakdown to occur with smaller applied voltages [67,68].

2.4.1 Mechanism

The mechanism of the electrical breakdown is highly complex, especially for solids, since it occurs in nanoseconds. Due to rapid occurrence, it is not easy to comprehend what is going on inside the lattice and follow the electron movement under certain applied voltage. However, there have been many studies and theories that the researchers have come up with in order to explain the mechanism. It is a time dependent event which can be classified as [65,69]:

- Electrical breakdown
- Thermal breakdown
- Electrochemical breakdown

There are other classifications regarding this phenomena in which the behavior of the electrons are taken into consideration:

- Avalanche breakdown
- Intrinsic breakdown

Even though there are different classifications, the basic principles of the failure mechanisms are very similar. When the applied voltage provides sufficiently large electrical field for electrons to jump over E_{gap} to conduction band, this leads to the breaking down of the material, electrically. Avalanche breakdown, on the other hand, as the name implies, explains the swarming of the electrons under applied voltage since there is non-zero probability for electrons to be in the conduction band, even for perfect insulating materials having large band gaps. Gathering enough energy from the electrical field, chain reaction starts and leads to a sudden increase in the current flow. Thermal breakdown, however, is somehow different than these mechanisms. During local heating of a small portion of the material under applied electrical field, the heat produced (locally) leads to increase in the defect concentration which subsequently favors the electrical breakdown. One should note that the rate (or the pulse) of the application of electrical field also affects the breakdown voltage [70–72].

CHAPTER 3

EXPERIMENTAL PART

In this work, in order to obtain homogeneous and dense oxide coatings on stainless steel substrate, ultrasonic spray pyrolysis deposition technique was used. The optimization of the process parameters have been done such as nozzle-to-substrate distance, temperature, spray area, solution concentration and scan speed. After obtaining the optimum process parameters, individual insulating oxide layers of SiO_2, Al_2O_3, MgO and TiO_2 were coated on AISI 304 stainless steel substrate followed by fluorine doped tin dioxide (FTO) layer on top of each layer. Since one of the main investigation is regarding electrical breakdown, the intermediate layers were focused deeply. Proper characterization techniques were used in order to understand the phenomenological behavior of the coated samples under applied voltage.

3.1 MATERIALS

Commercially available AISI 304 stainless steel plates (2 mm in thickness) were selected as the substrates and cut into square-shaped geometry using an abrasive cutter. The precursors used for FTO layer are tin (IV) chloride pentahydrate (Sigma-Aldrich, >98.0% $SnCl_4.5H_2O$) and ammonium fluoride (Sigma-Aldrich, >98.0% NH_4F). Prior to FTO layer, MgO, SiO_2, Al_2O_3 and TiO_2 intermediate layers were coated in which the precursors were selected as magnesium nitrate hexahydrate (Fluka, >99.0% $Mg(NO_3)_2.6H_2O$) for MgO, aluminum nitrate nonahydrate (Merck, >95.0%, $Al(NO_3)_3.9H_2O$) for Al_2O_3, tetraethyl orthosilicate (Sigma-Aldrich, >99.999% $Si(C_2H_5O)_4$) for SiO_2 and titanium (IV) iso-propoxide (Sigma-Aldrich, >97% $C_{12}H_{28}O_4Ti$) for TiO_2, respectively. Proper solvents that are required to dissolve these precursors are selected accordingly and summarized in **Table 3.1**.

Table 3.1 Table of the precursors used in film deposition, including solvents and desired yields with molarity.

Precursor Formula	Solvent	Molarity	Yield
$SnCl_4.5H_2O + NH_4F$	Methanol + DI water	0.1	FTO
$Mg(NO_3)_2.6H_2O$	Methanol	0.1	MgO
$Al(NO_3)_3.9H_2O$	Methanol	0.1	Al_2O_3
$Si(C_2H_5O)_4$	Methanol	0.1	SiO_2
$C_{12}H_{28}O_4Ti$	Methanol + isopropanol	0.1	TiO_2

3.2 DEPOSITION OF THE OXIDE LAYERS BY USP

Deposition of the oxide layers were obtained using ultrasonic spray pyrolysis method. Equipment used in this work is a basic setup which consists of a nozzle attached onto a stepper motor for x-y scanning (with adjustable speed) and a nebulizer (frequency of 1.63 MHz) that generates the mist from the spray solution, as shown in **Figure 3.1**. The generated mist that carries the fine droplets created by the nebulizer is blown onto the substrate. A heating plate is used in order to reach the desired temperature for the deposition and placed below the substrate. All of the substrates were prepared through proper metallographic preparation steps, grinded and polished until scratch-free mirror-like surface is obtained. Then they were ultrasonically rinsed in an alkaline solution for 45 min in order to satisfy the cleanliness of the surface.

Necessary amounts of the individual precursors are dissolved in appropriate solvent in order to obtain desired spray solution molarity. Only special solvent mixture was used for the TiO_2 deposition. The precursor used for TiO_2, which is titanium (IV) iso-propoxide, does not dissolve in methanol but in isopropanol. However, the mist could not be generated by isopropanol-based solution by the nebulizer since the power generated (frequency of 1.63 MHz) was simply not enough to break its bonds. In order to overcome this problem, methanol and iso-propanol was mixed so that it is enough

both for mist generation and dissolution of the precursor. The relative amount for this ratio was 1:1 for methanol and iso-2-propanol.

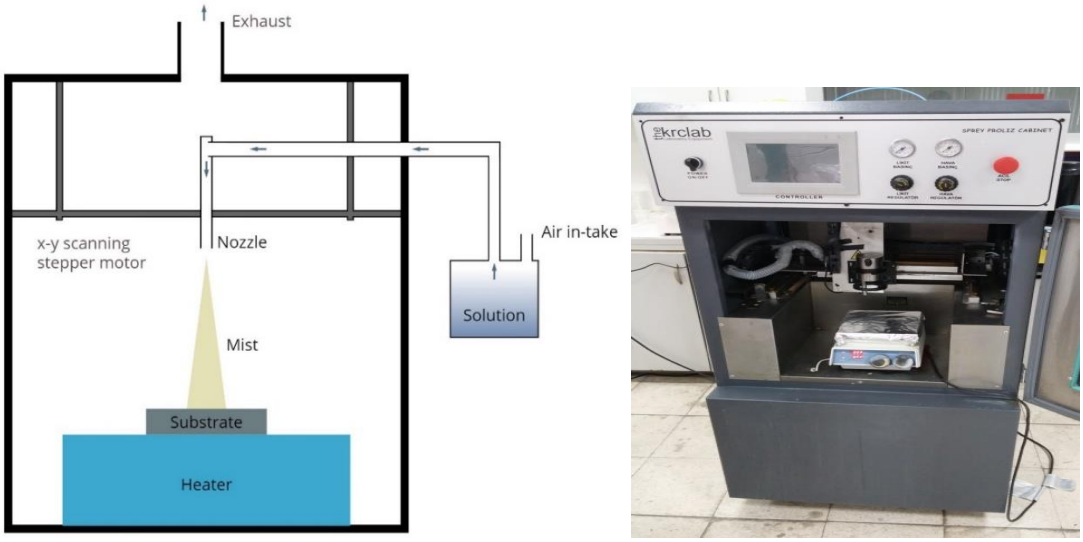

Figure 3.1 Schematic representation of the ultrasonic spray pyrolysis (USP) setup and USP equipment used in the experiments in Surface Science Research Laboratory.

Commercially available AISI 304 stainless steel substrates were used in this work. The chemical composition of the stainless steel used in this work is given in **Table 3.2**, which is in agreement with the standard composition of grade 304 stainless steels.

Table 3.2 Chemical composition of AISI 304 stainless steel substrate.

Composition of AISI 304 Stainless Steel (wt %)						
Fe	**C**	**Cr**	**Ni**	**Si**	**Al**	**Mn**
70.47 ± 0.15	0.07 ± 0.01	17.70 ± 0.17	9.33 ± 0.10	0.48 ± 0.01	<0.001	1.03 ± 0.01

The amount of the precursors used for each layer and the process parameters are summarized in **Table 3.3** which are, magnesium nitrate hexahydrate ($Mg(NO_3)_2.6H_2O$) for MgO, aluminum nitrate nonahydrate ($Al(NO_3)_3.9H_2O$) for Al_2O_3, tetraethyl orthosilicate ($Si(C_2H_5O)_4$) for SiO_2 and titanium (IV) iso-propoxide ($C_{12}H_{28}O_4Ti$) for TiO_2, respectively. For the FTO layer, the precursors were tin (IV) chloride pentahydrate ($SnCl_4.5H_2O$) as SnO_2 source and NH_4F as the fluorine, F, source.

Table 3.3 Solution preparation and process parameters determined for each layer, individually, *where: M: methanol, I: isopropanol, NSD: nozzle-to-substrate distance*.

Deposited Layer	**Precursor Weight (g)**	**Solvent used**	**Scanning Area (cm^2)**	**Scan Speed (cm/s)**	**NSD (cm)**	**Temperature (^oC)**
Al_2O_3	7.50	M	16	1	4.5	500
SiO_2	4.16	M	16	1	4.5	500
MgO	5.12	M	16	1	4.5	500
TiO_2	5.70	1:1 (M:I)	16	1	4.5	500
FTO	3.5	M	16	1	4.5	500

Each spray solution was ultrasonically rinsed for 30 min in order to obtain crystal-clear solution ensuring complete and homogeneous dissolution. Spray solution is then fed into the nebulizer and sprayed onto the pre-heated substrate. The substrate temperature for all the layers was kept constant at 500 ^oC.

3.3 DEPOSITION OF FTO LAYER

The precursors used in the deposition of FTO layers are tin (IV) chloride and ammonium fluoride. In order to reach the desired molarity for the spray solution, 3.5 g of tin (IV) chloride is mixed with 100 mL methanol and stirred until clear solution is obtained. In another beaker, desired amount of ammonium fluoride is mixed with 10 mL DI water and stirred until all the precursor is dissolved. After solving both precursors, they are mixed together that yields 0.1 M of spray solution. Final solution is again ultrasonically rinsed until it became crystal-clear. These specific amounts of the precursors were determined by the previous works that have been conducted in Surface Science Research Laboratory and it was found that minimum resistivity of the FTO films were obtained using the stoichiometric ratios of F/Sn as 1.5 atomic ratio. In this work, it was found that the resistivity of the FTO films decrease as F/Sn ratio increases from 0 to 2.7 [35]. However, after increasing F/Sn ratio further, the resistivity also increases. It is essential to obtain optimum resistivity to maximize the current flow so that the highest-possible efficiencies would be obtained. In order to do that, amount of doping has to be optimized as well as other process parameters.

When the spray solution is fed into the nebulizer, the spray mist is generated. The mist is, then, carried by air and blown onto the pre-heated substrate. When the mist meets the substrate surface, the pyrolytic reaction occurs that is mostly decomposition, leads to a uniform and high quality films. The pyrolytic reaction of the FTO layer, for example, is as follows:

$$NH_4F \rightarrow NH_3\,(\uparrow) + HF\,(\uparrow)$$

$$SnO_2\,(\downarrow) + 4HF \rightarrow SnF_4\,(\uparrow) + H_2O(\uparrow)$$

The side products NH_3, HF, SnF_4 and H_2O are exhausted from the system. The growth rate of the FTO films, as clearly seen from the reactions taking place, is mainly controlled by the HF concentration, which is determined by the NH_4F content initially. When F content is too high, for example, possible secondary reactions take place between growing SnO_2 and HF, hence the overall growth rate is hindered [21].

Spray solution that is prepared to deposit FTO, 100 mL, was enough to achieve desired resistivity values. After every single cycle, additional 1 min is provided to the system so that the settlement of the deposited layer was ensured. After each deposited layer, the resistance values of the FTO was measured so that the deposition could be stopped when desired resistance was obtained. When the deposition is completed, the heater was turned off and left to be cooled slowly inside the chamber until it reached to the room temperature. Obtaining dense, homogeneous and high-quality deposition of FTO layer made it possible for further characterizations and heating experiments accordingly which is explained in detail in the upcoming sections.

3.4 BREAKDOWN VOLTAGE MEASUREMENTS

As explained in the previous chapter, the breakdown voltage (BDV) measurements for each individual layer was conducted as shown in **Figure 3.2**. In order to disregard the effect of the substrate temperature over breakdown voltage values, the voltage applied was in contact with the substrate for a short amount of time like a pulse (<1 s). Again, the voltage values were increased step-by-step while measuring the current flow. After certain amount of applied voltage, the coating could not carry the voltage and simply electrically broke down. Similar to what happened in the heating experiments, a sudden jump in the current flow to much higher values, makes it much easier to understand at which the applied voltage value exceeds the BDV of the material. The data obtained is then plotted as applied voltage (V) vs current flow (A).

Also, the effect of temperature dependency of BDV was investigated. For this purpose, the substrate was placed above a heating-plate and same experiment explained above was repeated for several set of temperatures (from room temperatures to 400 ^{o}C). It is essential to understand the temperature dependency of this phenomena since it is one of the major factors that effects the BDV value of a material under consideration, drastically.

3.5 HEATING EXPERIMENTS

After successful deposition of the layers, the obtained samples were subjected to heating experiments. The setup is rather simple that consists of a voltage and current supplier (YOKOGAWA GS610) which is attached and in contact with the substrate using two silver paste contacts 1 cm apart from each other. For the temperature measurement, K-type thermocouple was also connected onto the substrate surface. The experimental setup is given schematically in **Figure 3.2**. The voltage was increased step-by-step and current flow and temperature values were recorded.

After setting the voltage, the value of the current flow was recorded until saturation temperature of the substrate was reached. The occurrence of breakdown can easily be observed by the sudden current change in YOKOGAWA GS610. For example, a steady current flow of 0.3 A is being measured under 5 V of applied voltage. After a while, with the help of increased temperature, the current flow suddenly jumps to 3.2 A, which is the current limit of the supplier. This indicates that the current is no longer flowing through the deposited layer above the substrate, but rather from the substrate below, which is a highly conductive material. All of the measurements regarding this phenomena was carefully conducted, accordingly.

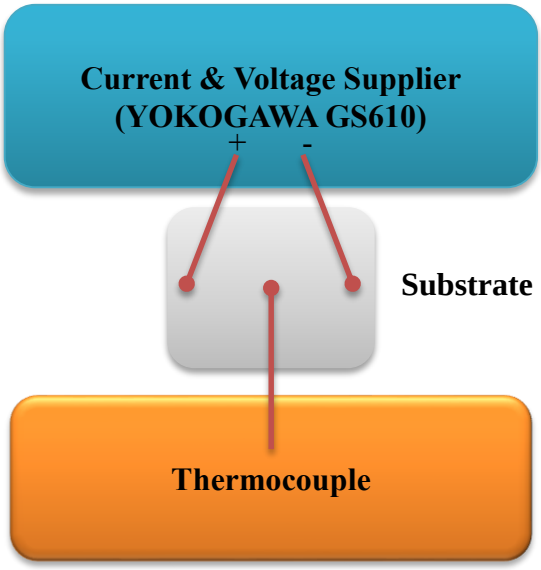

Figure 3.2 Schematic drawing of the experimental heating setup where substrate is attached to current/voltage supplier with K-type thermocouple.

3.6 SHEET RESISTANCE MEASUREMENTS

Sheet resistance (R_{sh}) is an important factor to determine the quality and electrical properties of the deposited thin films. In order to measure the sheet resistance values of the FTO deposited samples, JANDEL universal probe was used, as shown in **Figure 3.3**. Appropriate calculations to get proper and meaningful units for R_{sh}, which is ohm/sq or Ω/□, were done accordingly by using four-point probe measurement technique. Since sheet resistance is a special concept to determine resistivity for a uniform thickness, at the end, obtained sheet resistance values can also be used to determine the resistivity values of the films. This calculation is a simple one in which the sheet resistivity values are multiplied with the film thickness, yielding resistivity.

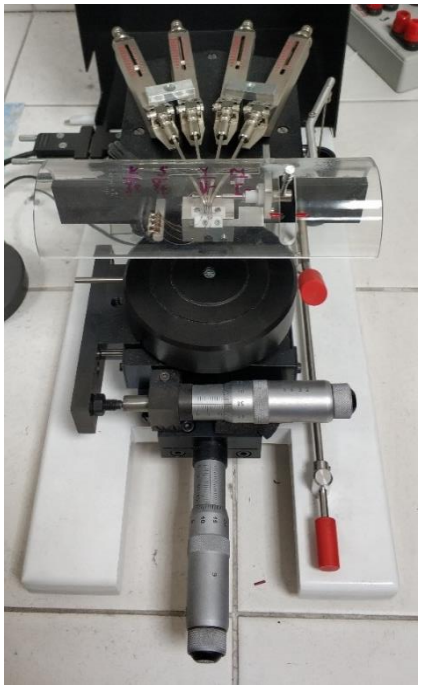

Figure 3.3 JANDEL universal probe used for sheet resistance (R_{sh}) measurements in Surface Science Research Laboratory of METE/METU.

3.7 SECONDARY CHARACTERIZATIONS

After preparing the spray solutions and deposited substrates, the coatings were investigated using a scanning electron microscope (SEM, FEI 430 NanoSEM) to understand the morphological properties of the films such as coating thickness, surface morphology and distribution of the deposited layer across the substrate. X-ray diffraction patterns of the samples, both before and after deposition, were obtained using Rigaku D/MAX 2200/PC X-Ray diffractometer. For further investigations such as surface roughness an atomic force microscopy (hpAFM Nanomagnetic Instruments) was used. Both 3D morphologies of the layers and average surface roughness values were obtained. Sheet carrier densities, carrier mobility and resistivity values were obtained using Hall probe technique (Lakeshore 7700A) in standard van der Pauw configuration.

3.8 HUMIDITY TEST

For the purpose of understanding the behavior of the samples under high humid environment, humidity test was conducted. The testing setup includes a chamber that is capable of supplying a stable 95% relative humidity. The temperature changes were programmed so that the range is between 20-60 ^{o}C with controllable steps. The test setup is a closed chamber and isolated from the ambient so that controllable testing conditions were satisfied. The test lasted ten days without any interruption and composed of five times repeating two day long routines (5 x 2 days) as shown in **Figure 3.4**.

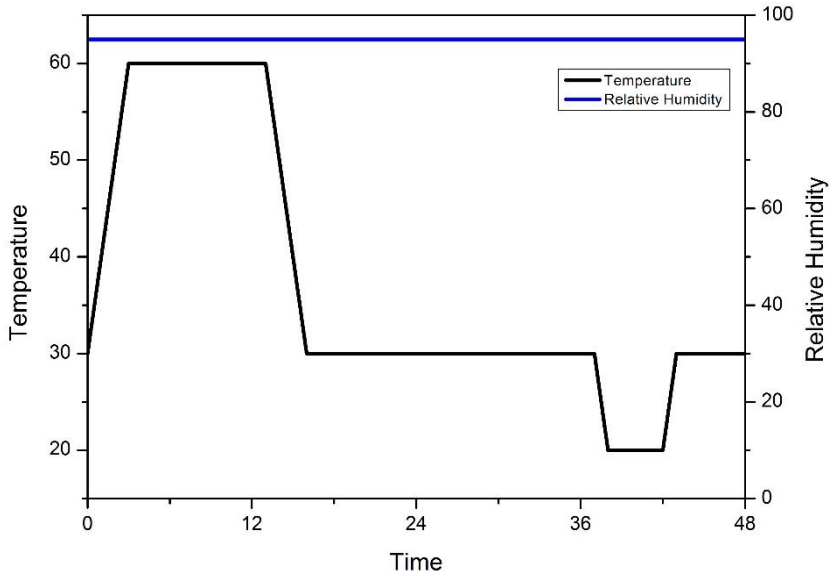

Figure 3.4 The 2 days humidity test routine applied in this study.

CHAPTER 4

RESULTS AND DISCUSSION

In this study, four different insulating oxide layers (SiO_2, Al_2O_3, MgO and TiO_2) were deposited in between FTO layer and stainless steel substrate, as shown in **Figure 4.1**. Having an insulating layer sandwiched between the substrate and FTO enables to reach higher temperatures by simply having more capability to work under an applied voltage. In order to understand this increase, all of the intermediate layers were investigated and compared with each other using several characterization techniques. After determining the best possible intermediate layer, FTO was deposited afterwards and heating experiments were conducted.

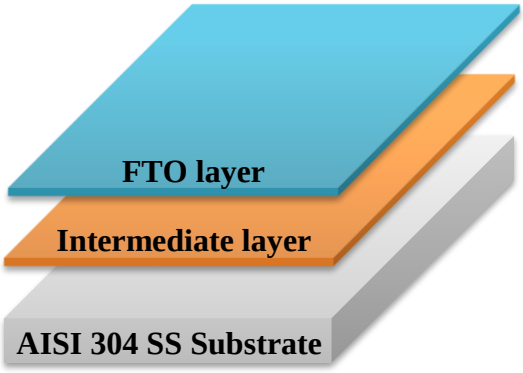

Figure 4.1 Schematic representation of the sandwiched structure of insulating layer (SiO_2, Al_2O_3, MgO or TiO_2) in between FTO layer (above) and AISI 304 stainless steel substrate (below).

4.1 SEM CHARACTERIZATION OF THE LAYERS

All of the intermediate layers coated using USP method were properly prepared for further SEM investigations. In order to provide sufficient electrical conductivity, all of the samples were coated by gold using sputtering technique. Both cross-sectional and surface investigations were carried out using SEM. Also, elemental analysis were conducted using EDS in order to obtain information about the stoichiometric ratios of the elements which are the constituents of the oxide compound above the substrate surface. Despite the efforts, only titania, TiO_2, layer was successfully formed a homogeneous and continuous coating on the stainless steel substrate while others failed to show such continuous film growth. The deposition of other oxide layers than TiO_2, was not successful since either the wetting conditions between the substrate and the precursor used was not suitable or the temperature was not sufficiently high for film growth mechanisms. The resulting morphology of these intermediate layers showed simply as particulates with various sizes. Among the failed oxide layers, only MgO showed only a small amount of layer growth while, again, showing particulated-growth quickly after the layer formation. Titania, on the other hand, showed a remarkable layer growth on AISI 304 stainless steel substrates. The detailed microstructural investigations regarding these layers are given in the upcoming sections.

4.1.1 Alumina Layer

Alumina, Al_2O_3, was coated on stainless steel substrate prepared by USP, as seen in **Figure 4.2**. There is almost no film grown on the substrate surface but there exist islands and/or particulates with various sizes across the substrate surface. The morphology indicates that the wetting conditions using nitrate-based precursors were not sufficient for film growth. Although theoretically alumina has promising insulating properties, since no layer formation occurred using nitrate-based precursors, one can conclude that it is not suitable for the purpose of this work.

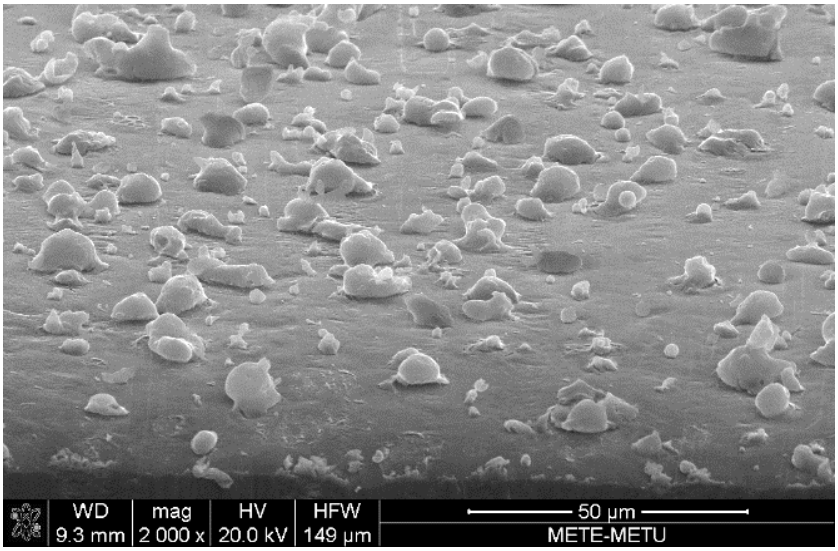

Figure 4.2 SEM image of Al_2O_3 coated AISI 304 stainless steel substrate prepared by USP.

4.1.2 Magnesia Layer

Magnesia, MgO, was coated on stainless steel substrate prepared by USP. Compared to Al_2O_3, the morphology is slightly different. However, even though there is a very thin layer formed above the substrate surface, there are still MgO islands and/or particulates across the surface with various sizes as seen in **Figure 4.3**. The thin layer formed increased the breakdown voltage (BDV) as expected, however, the impact of the increase was not so important since the thickness of the MgO layer is well below 50 nm.

There are several studies that focused on MgO coatings on stainless steel substrates with different precursors used. Shadi et.al. reported that the deposition was done using different precursor agents which are acetate-based and nitrate-based precursors using USP method with 550-750 ^oC ranges on AISI 321 stainless steel. The findings showed that the nitrate-based precursors were not successful due to wetting environment. It was reported that only an amorphous layer of MgO existed which was confirmed by EDS with the ratio of 0.3:0.7 [73]. In their study, the substrates used were 312-

austenitic and the same wetting problem was observed since the precursor was nitrate-based.

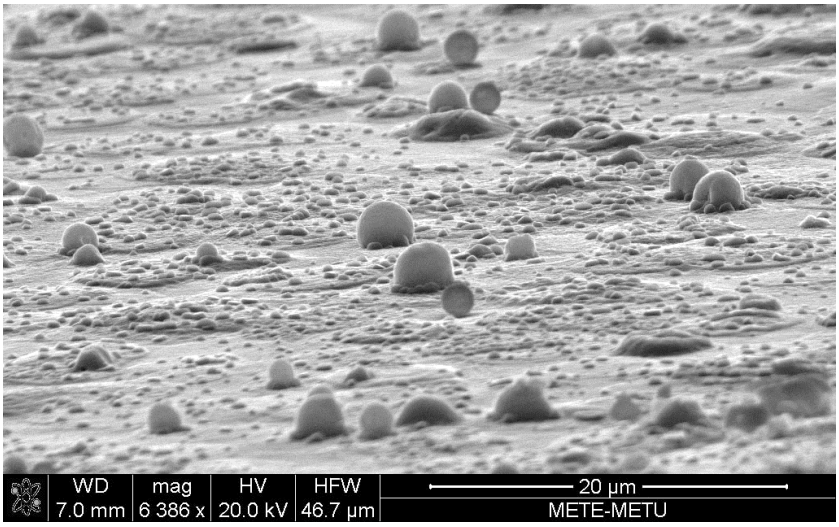

Figure 4.3 SEM image of MgO coated AISI 304 stainless steel substrate prepared by USP.

It can be said that the islandic growth of MgO is favorable under these deposition conditions using USP technique which results in a micron and sub-micron islands and particulate sizes plus a very thin layer (<50 nm) formed above the substrate surface as seen in the enlarged image which is shown in **Figure 4.4**. Although there is a thin layer formation, it is still not suitable and insufficient for the purpose of this work.

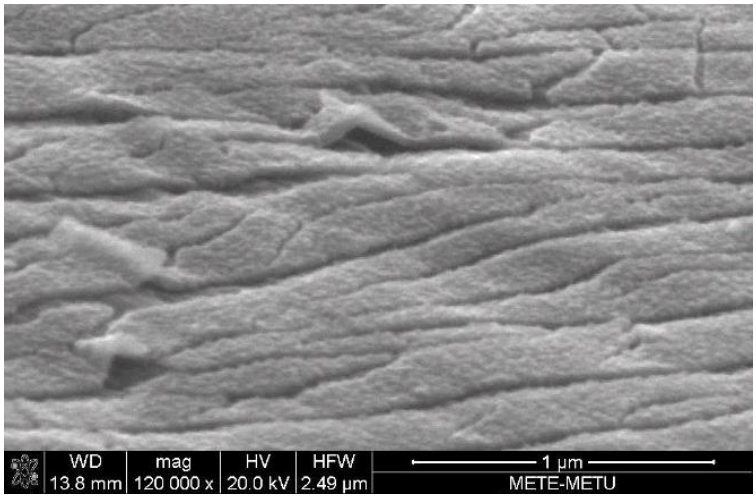

Figure 4.4 SEM image of MgO coated AISI 304 stainless steel substrate prepared by USP.

4.1.3 Silica Layer

Silica, SiO_2, was coated on stainless steel substrate prepared by USP, as seen in **Figure 4.5**. The resulting morphology is very similar to Al_2O_3. As seen from the SEM image, there is no film growth on the stainless steel surface. Only micron-sized islands/particulates exist within the morphology which can be, again, attributed to wetting environment of the precursor used. The precursor used for silica was tetraethyl orthosilicate ($Si(C_2H_5O)_4$) which only provides particulate/island growth of silica across the stainless steel substrate. Due to the fact that no layer formation occurred, SiO_2 was also eliminated since it has no contribution to electrical breakdown studies.

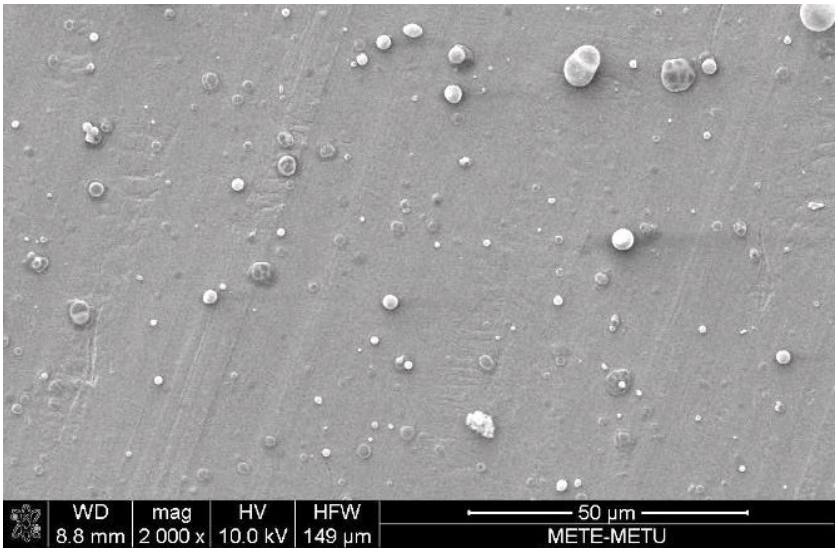

Figure 4.5 SEM image of SiO_2 coated AISI 304 stainless steel substrate prepared by USP.

4.1.4 Titania Layer

Among all of the above-mentioned oxide layers, only titania, TiO_2, was successfully grown on AISI 304 stainless steel substrate using titanium (IV) iso-propoxide precursor. Only problematic issue with preparing spray solution was that the methanol was not dissolving titanium (IV) iso-propoxide. In order to overcome this, additional isopropanol was used in mixture with methanol since isopropanol is a suitable solvent for the precursor. However, another problem arises in this condition since the power

generated by the nebulizer (1.63 MHz) was not enough to break propanol-based solutions, therefore the mist could not be obtained using propanol-based solutions. Therefore, the proper ratio of these solvents was required to be found so that dissolution of the precursor should be satisfied as well as the mist generation is sufficient enough to wet the substrate surface. Methanol-to-isopropanol ratio was found to be 50:50 by volume so that both issues were solved and TiO_2 was successfully coated on AISI 304 stainless steel substrate. Five samples were prepared with different thickness values as given in **Table 4.1**.

Table 4.1 EDS analysis of the TiO_2 coated samples (T1, T2, T3, T4 and T5) prepared by USP.

Sample Label	Thickness (nm)	Ti (At. %)	O (At. %)	Ti/O Ratio
T1	85 ± 35	0.98	7.08	0.14
T2	130 ± 25	2.40	8.61	0.28
T3	165 ± 10	4.23	11.34	0.37
T4	265 ± 25	6.48	12.75	0.54
T5	670 ± 15	18.21	30.05	0.61

As seen from **Figure 4.6**, the surface morphology of TiO_2 is highly dense, homogeneous and well dispersed across the substrate surface. The thickness of the films were also investigated. For this purpose, five different samples were prepared with different thickness values (labeled as T1, T2, T3, T4 and T5). In order to identify the thickness of the films, the samples were cut in half and mounted into bakelite vertically. Proper grinding and polishing were performed on the cross-sectional surface of the samples.

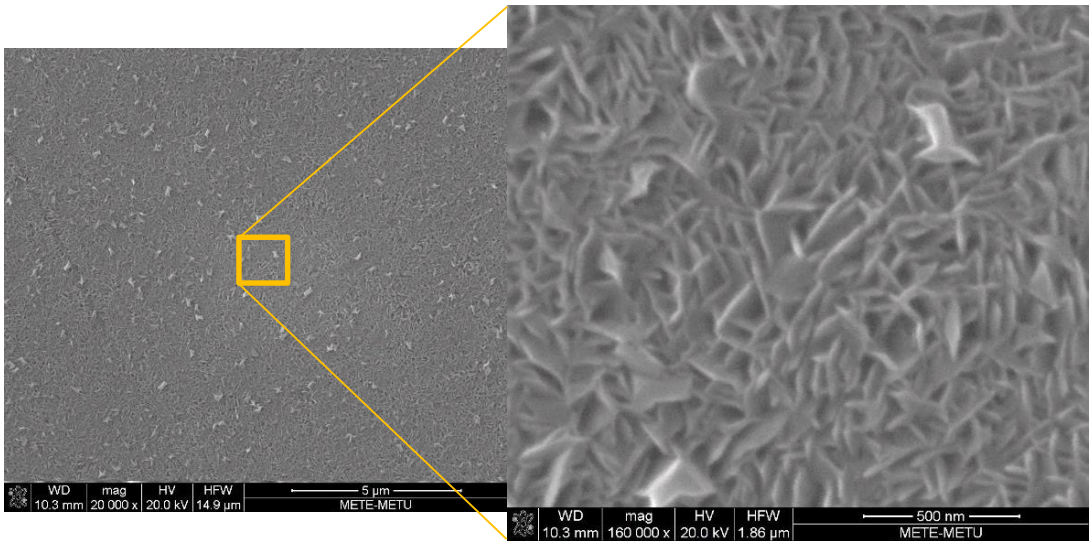

Figure 4.6 SEM image of TiO_2 coated AISI 304 stainless steel substrate prepared by USP.

The cross-sectional SEM image of TiO_2 coating is given in **Figure 4.7**. The bakelite part of the mounted sample can be seen from the figure as well, where it is the upper part of the SEM image. The maximum thickness of coating was ~670 nm with homogeneous distribution throughout the substrate surface under these given preparation and process conditions. After reaching to a critical thickness value, the mist generated from the spray solution tends to particulate on the coated surface which makes it not possible to grow any layer further. SEM images of samples T3, T4 and T5 with different coating thicknesses is given in **Figure 4.8**.

Individual EDS analysis results of TiO_2 coated samples T1, T2, T3, T4 and T5 are given in **Figure 4.9**. As expected, the signals of both oxygen and titanium were increasing with increasing coating thickness. Relative amounts of these elements were also summarized in **Table 4.1** including film thickness values. Combining EDS results with SEM results, it was concluded that the TiO_2 layer was formed on AISI 304 stainless steel substrate using USP successfully.

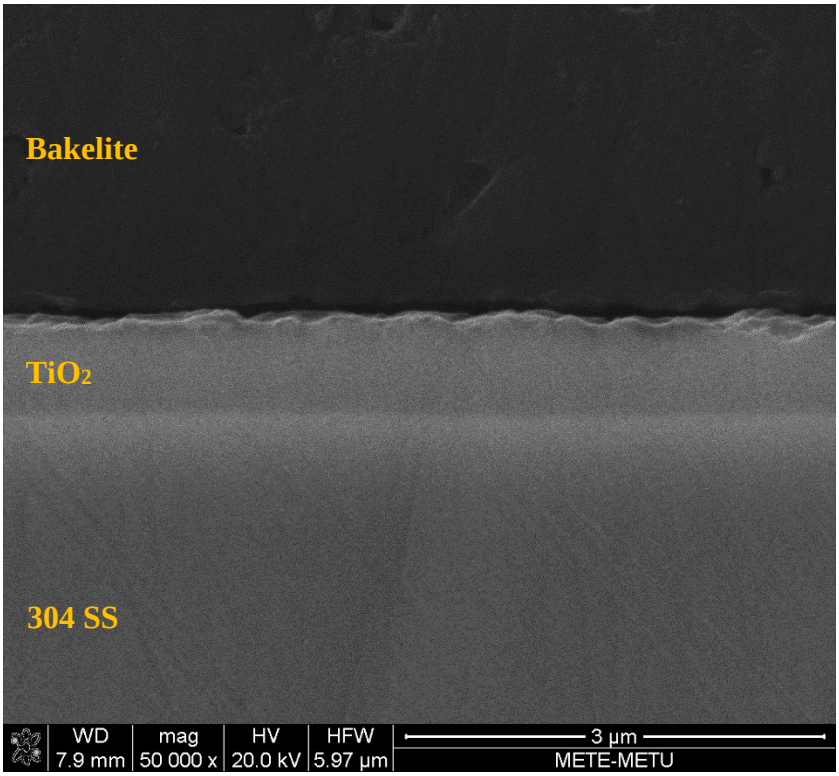

Figure 4.7 Cross-sectional SEM image of TiO_2 (T5) coated AISI 304 stainless steel substrate prepared by USP.

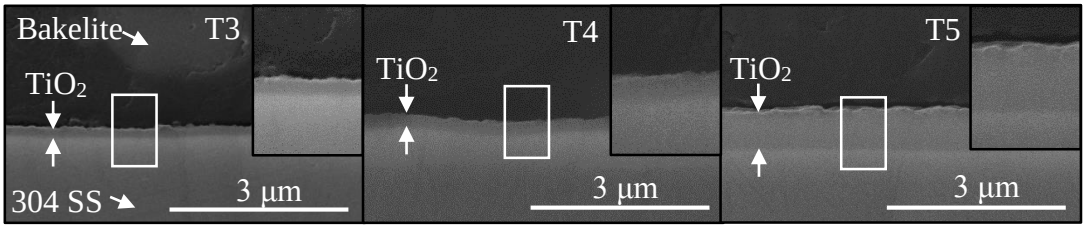

Figure 4.8 Cross-sectional SEM images of TiO_2 (T3, T4 and T5) coated AISI 304 stainless steel substrates prepared by USP.

Due to homogeneity and continuity of TiO_2 layer prepared by ultrasonic spray pyrolysis on AISI 304 stainless steel substrate, TiO_2 was selected as the intermediate insulating layer.

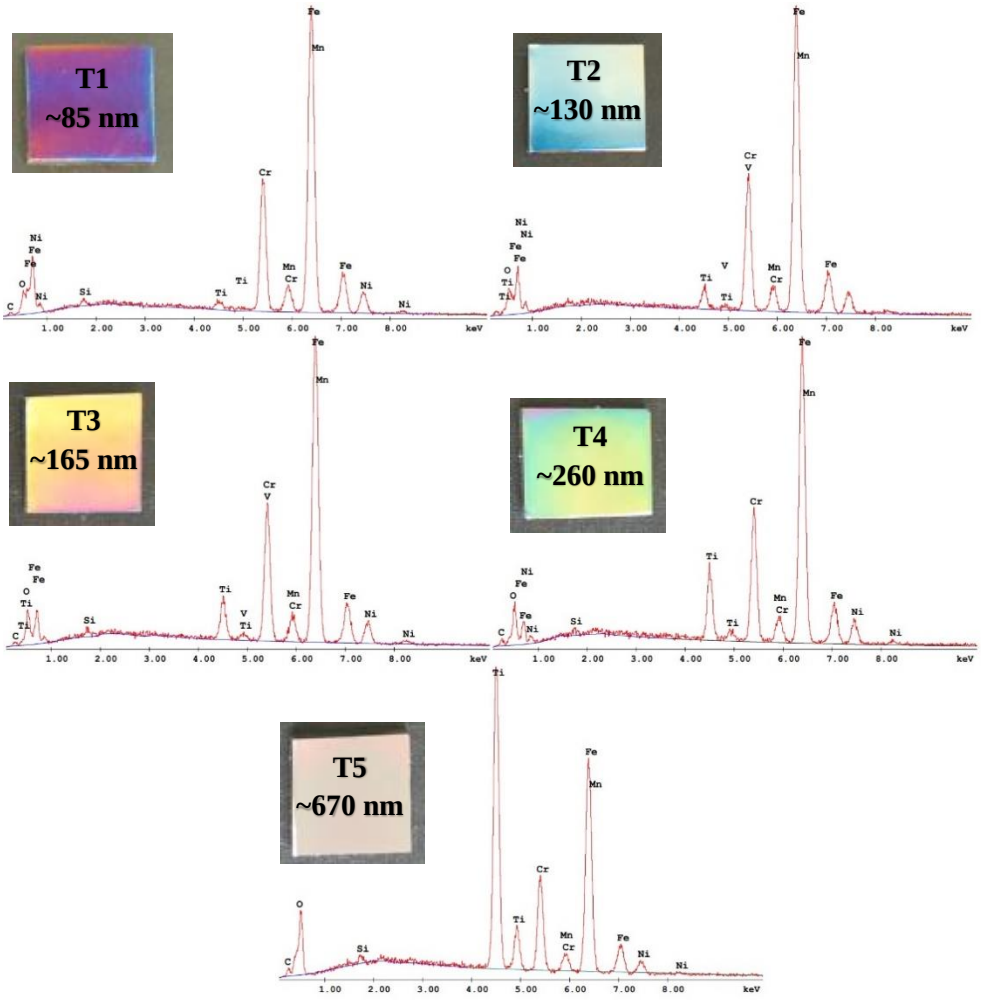

Figure 4.9 Elemental analysis of samples T1, T2, T3, T4 and T5 TiO_2 coatings deposited on AISI 304 stainless steel substrate prepared by USP.

4.1.5 FTO Layer

FTO was coated on AISI 304 stainless steel substrates using USP. Both thickness measurements and surface morphology of the FTO layer were investigated through SEM analysis. As can be seen in **Figure 4.10**, the homogeneity and dense structure of FTO over stainless steel substrate was well established. The thickness was homogeneous throughout the structure with some slight deviations. Changing the number of spray cycles, it is possible to alter the coating thickness where ~280 nm, ~300 nm and ~520 nm coating thicknesses for FTO layers were achieved.

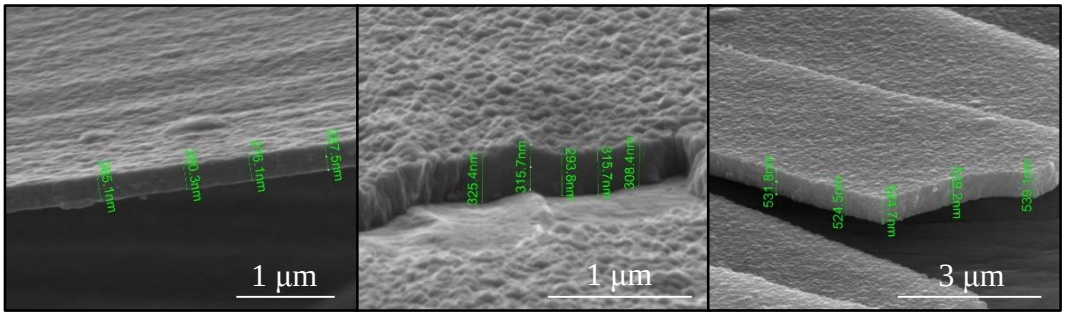

Figure 4.10 SEM images of FTO coated AISI 304 stainless steel substrates prepared by USP.

The images were taken close to the part where the sample was cut. Because of that, the FTO coating showed discontinous behavior whereas the remaining parts shows highly dense, continous and homogeneous morphology throughout the surface. To investigate the thickness values, the samples were cut hence the coating was, unintentionally, ripped off from the surface so that the cross-sectional morphology was revealed.

4.1.6 FTO Layer with Intermediate Oxide Layers

Deposition of FTO on top of each oxide layer was achieved using same process parameters. Even though the SEM examinations revealed that MgO, SiO_2 and Al_2O_3 coated samples did not form any continuous layer, FTO layers were deposited and examined. As seen in **Figure 4.11**, the particulates remaining over the surface were also coated with FTO during deposition. However, since there is no film grown below FTO layer, the separation of FTO layer and stainless steel surface was not obtained. Hence, one should not expect any increase in the BDV values of these samples. Even though, theoretically, especially MgO, offers remarkable insulation properties that would be greatly helpful for solving this problem, obtaining only particulates on the surface showed that it is not possible under these coating conditions and precursors involved in the process.

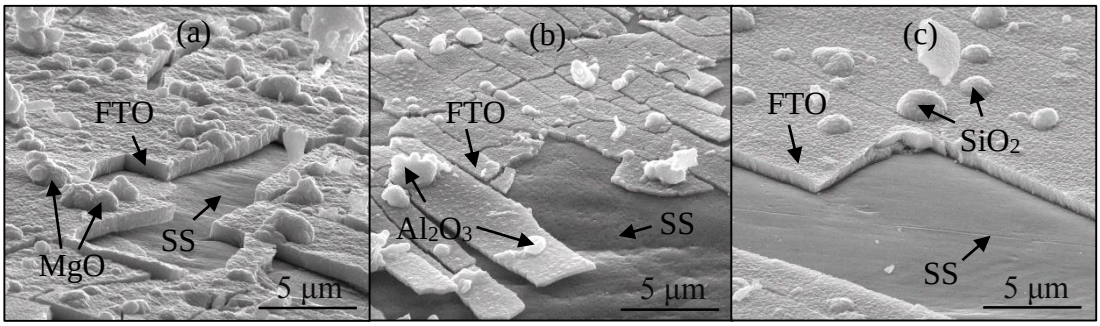

Figure 4.11 SEM images of FTO coatings with (a) MgO, (b) Al_2O_3 and (c) SiO_2 intermediate layers on AISI 304 stainless steel substrates prepared by USP.

TiO_2, on the other hand, showed remarkable coverage across the surface. The SEM analysis has already confirmed that the homogeneous film growth was achieved. Also, there was no problem during deposition of FTO layer above TiO_2 coated AISI 304 stainless steel substrate. Hence, five different FTO layers with different sheet resistance values were deposited on TiO_2 coated SS substrate with similar TiO_2 thicknesses, labeled as TF1, TF2, TF3, TF4 and TF5, as shown in **Table 4.2**.

Table 4.2 The characteristics of FTO coated samples with intermediate TiO_2 layers prepared by USP.

Sample Label	Thickness (nm)		F/Sn Ratio (At.)
	TiO_2	FTO	
TF1	660 ± 25	160 ± 20	1.5
TF2	660 ± 60	350 ± 40	1.5
TF3	600 ± 30	310 ± 30	0.2
TF4	770 ± 20	150 ± 10	0
TF5	620 ± 20	260 ± 15	0
TF6	660 ± 25	160 ± 20	2.7

The surface of the FTO coated AISI 304 stainless steel substrate with TiO_2 intermediate layer is given in **Figure 4.12**. As seen in the SEM image, the deposited FTO coating above the intermediate layer is dense, homogeneous and well-distributed with its grain size is in nano-size range.

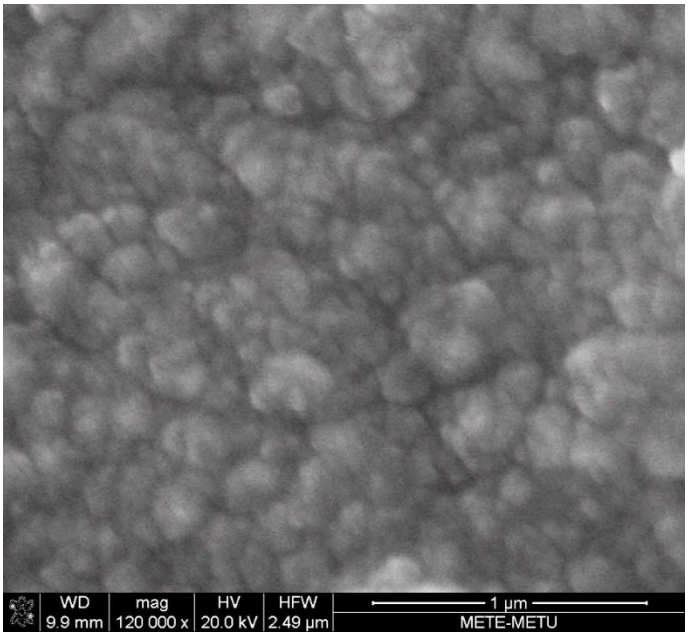

Figure 4.12 SEM image of FTO coated AISI 304 stainless steel substrate with TiO_2 intermediate layer sandwiched in between prepared by USP.

The morphology of FTO growing on TiO_2 was similar to that of growing on bare stainless steel. However, these two oxide layers were not easily be distinguished using SEM. TiO_2 and FTO layers showed similar contrast under investigation, hence this made it quite difficult to determine individual thickness values. In order to overcome this problem, back-scatter mode of SEM was used to distinguish these oxide layers from each other. Also, using EDS-mapping has confirmed the existence of individual layers.

As seen in **Figure 4.13**, the individual layer thicknesses of TiO_2 and FTO layers are almost indistinguishable and concluding thickness values using secondary electron image can lead to a misleading result. The back-scatter electron image yields much higher contrast between layers since its working principle is based on the atomic number difference. Hence, higher the atomic number difference higher the contrast.

Since the elements titanium and tin exist within those layers which have atomic number of 22 and 50, respectively, it is expected to observe such contrast. With the help of this method, much precise thickness measurements were obtained for individual layers for the samples.

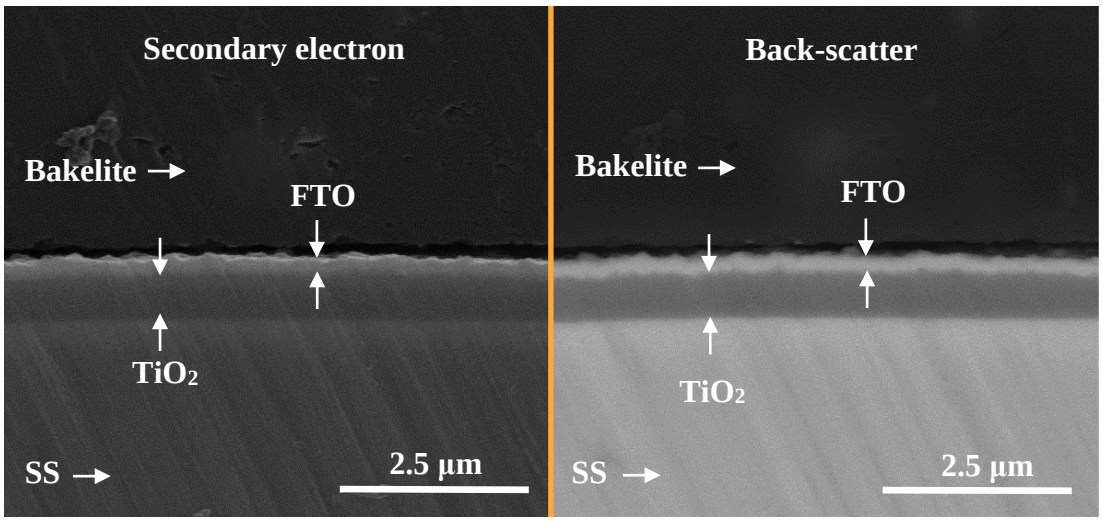

Figure 4.13 Secondary electron image (left) and back-scatter electron image (right) of FTO coated AISI 304 stainless steel substrate with TiO_2 intermediate layer (TF5) prepared by USP.

Also, results of EDS-mapping which are given in **Figure 4.14** indicate that these layers were successfully deposited on AISI 304 stainless steel substrate using ultrasonic spray pyrolysis. Double layered structure can be observed by combining the images, given in **Figure 4.15**. The noise in the data may arise from the fact that these samples were cut, ground and polished before SEM examination. Therefore, undesired residual particles may have been distributed throughout the cross-section.

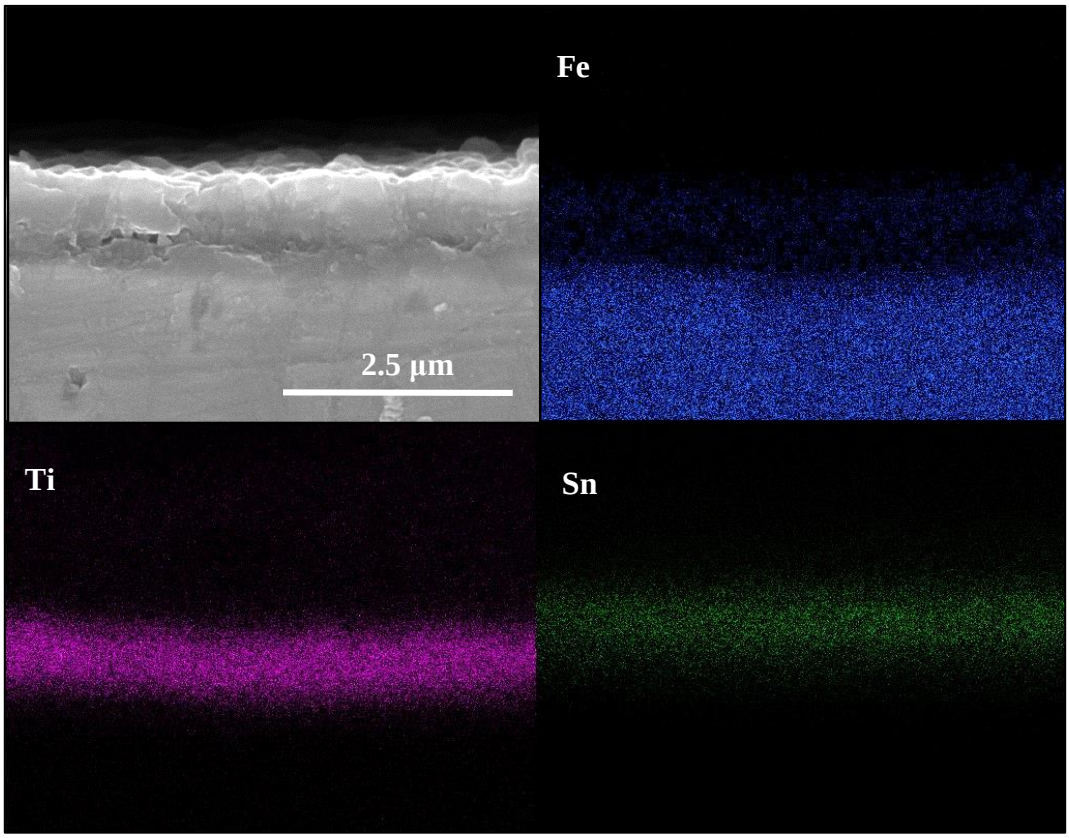

Figure 4.14 EDS mapping of FTO coated AISI 304 stainless steel substrate with TiO_2 intermediate layer (TF2) prepared by USP, where blue, purple and green points represent Fe, Ti and Sn, respectively.

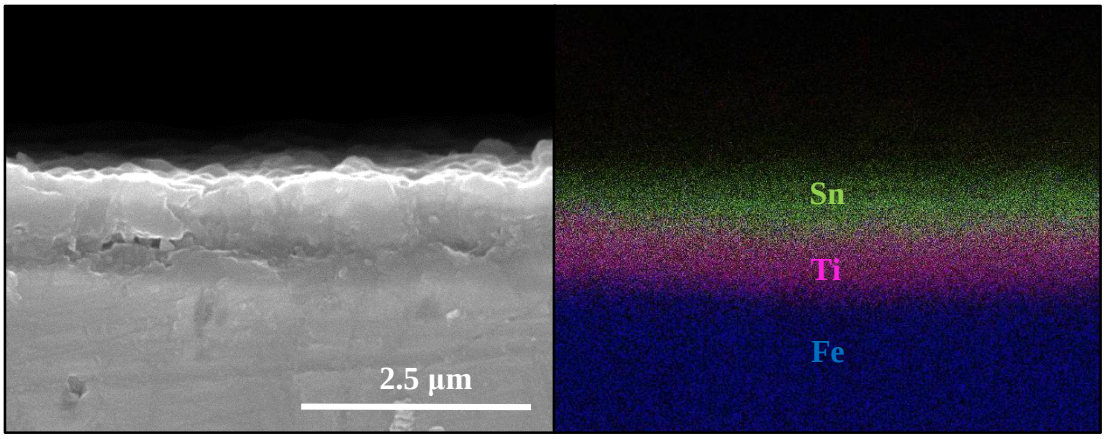

Figure 4.15 EDS mapping (combined) of FTO coated AISI 304 stainless steel substrate with TiO_2 intermediate layer (TF2) prepared by USP, where blue, purple and green points represent Fe, Ti and Sn, respectively.

4.2 XRD ANALYSIS OF THE COATED SAMPLES

Since SiO_2, MgO and Al_2O_3 coatings did not form any films, only very small intensity peaks or almost no peaks were observed in their XRD patterns respectively as shown in **Figure 4.16**.

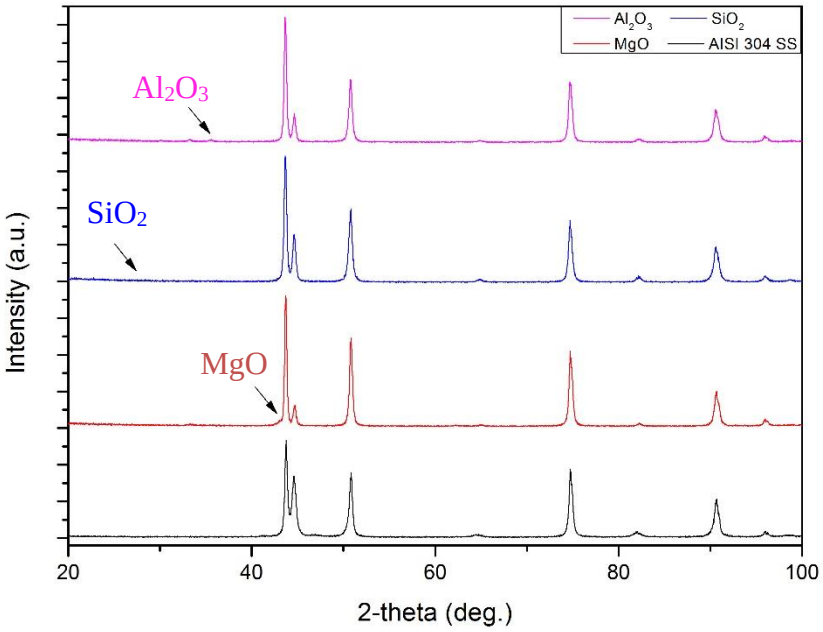

Figure 4.16 XRD patterns of Al_2O_3, SiO_2 and MgO coated AISI 304 stainless steel substrates prepared by USP.

The main peaks of Al_2O_3, MgO and SiO_2 were expected to be around 35°, 43° and 27°. The peaks of Al_2O_3 and SiO_2 were barely visible or non-existent in the spectra being suppressed by the instrumental noise and simply due to the fact that there exists almost no film formation on the surface. A very thin film formed in the case of MgO, on the other hand, was apparent in the pattern. However, since the main peak of the substrate used for these coatings slightly overlaps with that of MgO peak, a small shoulder on the left-hand-side of the substrate peak at 43° was observed at which the crystallographic planes for MgO and AISI 304 SS are (200) at 42.8° and (111) at 43.7°, respectively.

XRD pattern of bare AISI 304 stainless steel (SS) used as substrate material for the depositions in this work is given in **Figure 4.17**. α-Fe corresponds to martensitic part of the stainless steel. AISI 304 is an austenitic stainless steel, however stress induced martensitic transformation might occur during processing of steel to form plate-like geometries. The existence of the martensitic phase seen in the XRD pattern of the substrates indeed proves the occurrence of stress induced martensitic transformation.

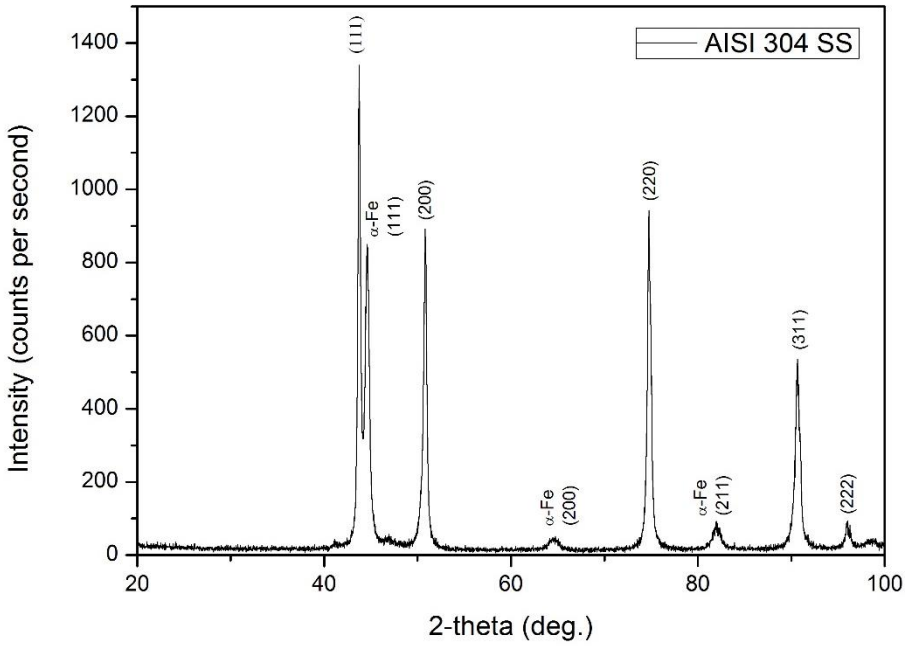

Figure 4.17 XRD pattern of bare AISI 304 stainless steel used as the substrate material for the depositions.

XRD pattern of TiO_2 coating on AISI 304 stainless steel is given in **Figure 4.18**. There exists only a very small, almost negligible, amount of rutile phase present in the film, at 70^o labeled as Rutile (301), while the remaining part of the film mostly consists of the anatase form of TiO_2. As explained earlier, anatase is the tetragonal form of TiO_2 which forms along the surface of stainless steel substrate. Reporting no any other phases proves that the deposition of TiO_2 layer was successfully performed on the substrate. The preferential growth of TiO_2 on the stainless steel substrate is alone (101) and (200) which corresponds the lowest surface energy planes that explains the preferential film growth.

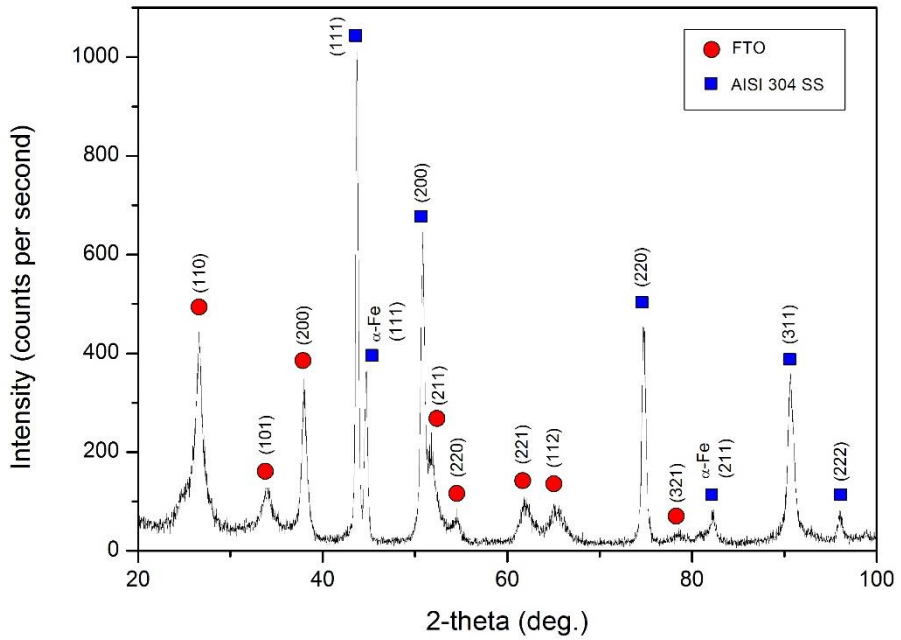

Figure 4.18 XRD pattern of TiO_2 coating deposited on AISI 304 stainless steel prepared by USP.

Compared to growth of TiO_2 on AISI 304, FTO grows preferentially along (110) and (200) planes as seen in the XRD pattern of FTO coating given in **Figure 4.19**.

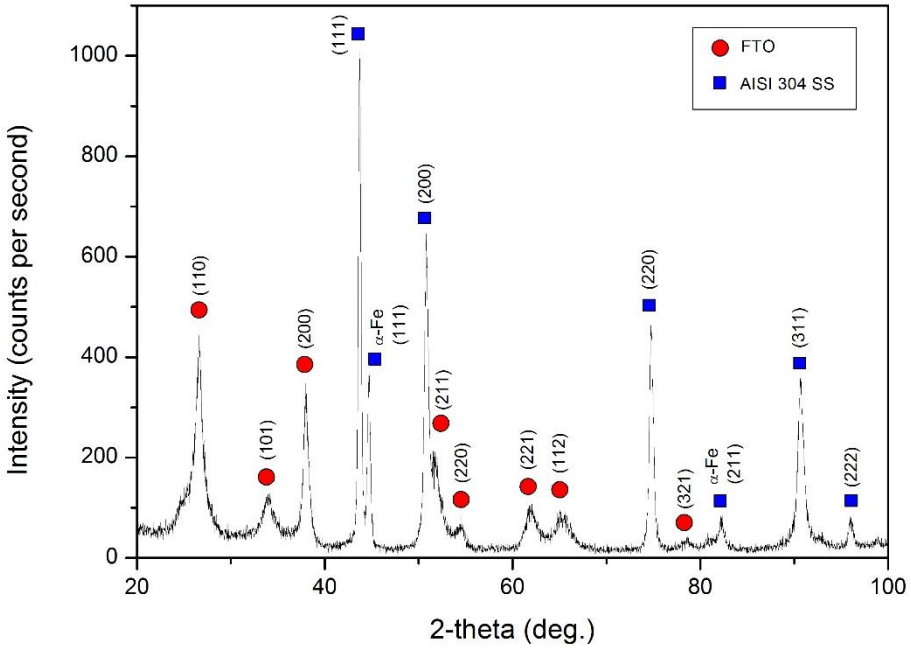

Figure 4.19 XRD pattern of FTO coating deposited on AISI 304 stainless steel prepared by USP.

Even though the lowest energy plane of FTO is (200), since many other parameters such as lattice matching with the substrate, temperature and pressure are included, the growth of this plane is in competition with (110) plane. This can simply be explained by the lattice matching between FTO and the stainless steel substrate which favors (110) growth due to stainless steel being in the form of face-centered cubic (FCC) structure. XRD pattern of FTO deposited AISI 304 stainless steel substrates with TiO_2 intermediate layer prepared by USP is given in **Figure 4.20**. Because of the preferential growth kinetics, it can be seen that (101) growth of TiO_2 ultimately affected the growth of same oriented plane (101) growth of FTO layer above the intermediate layer. Reporting no any other undesired phases present in the XRD spectra showed that all the deposition processes, including growing FTO on TiO_2 coated SS, were successfully achieved. Combined XRD patterns of the above-mentioned samples were given in **Figure 4.21**.

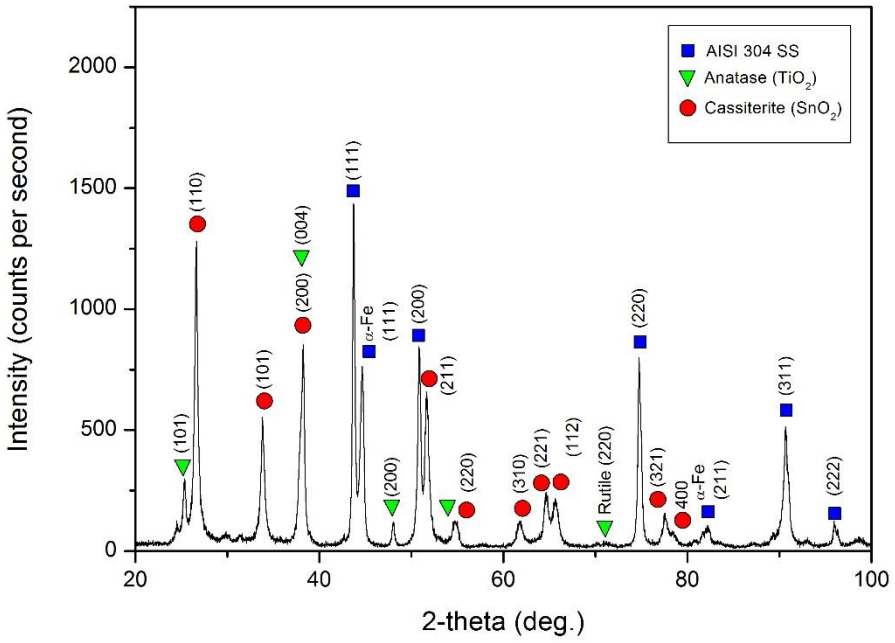

Figure 4.20 XRD pattern of FTO coating deposited AISI 304 stainless steel substrates with TiO_2 intermediate layer prepared by USP.

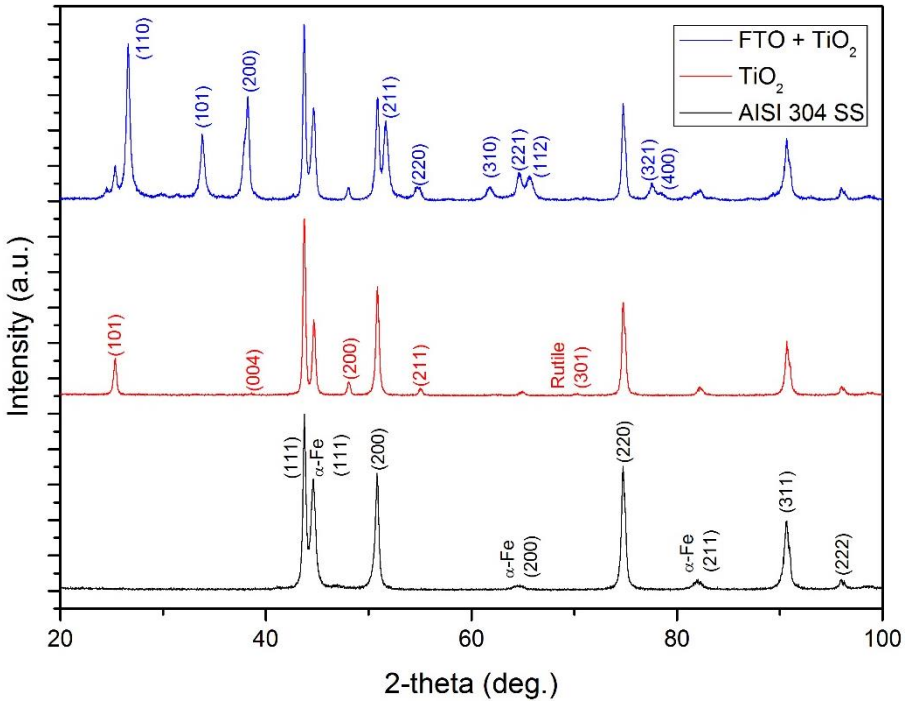

Figure 4.21 XRD patterns of bare AISI 304 stainless steel (at the bottom), TiO_2 coated SS (in the middle) and FTO coated SS with TiO_2 intermediate layer (at the top), prepared by USP.

According to all investigations done using XRD enabled calculation of individual lattice constants for AISI 304 SS (face centered cubic structure) with TiO_2 and FTO coatings prepared by USP. Since TiO_2 and FTO layers exhibit tetragonal structure, the lattice parameter calculations for these layers were different. Using Bragg's Law:

$$\lambda = 2d\sin\theta \qquad \text{[Eq. 4.1]}$$

for cubic:

$$\frac{1}{d_{hkl}^2} = \frac{h^2+k^2+l^2}{a^2} \qquad \text{[Eq. 4.2]}$$

and for tetragonal crystal structure:

$$\frac{1}{d_{hkl}^2} = \frac{h^2+k^2}{a^2} + \frac{l^2}{c^2} \qquad \text{[Eq. 4.3]}$$

lattice constants of a and c can be calculated where λ is 1.54056 Å (Cu K_α), d is interatomic distance, θ is diffraction angle and h, k and l represent miller indices. The results of these calculations are given in **Table 4.3**, which also includes some data from the literature.

Table 4.3 Lattice constants for TiO_2 and FTO prepared by USP and SS substrate, compared with previous studies and their coefficient of thermal expansion values.

Sample	Lattice Constants				Coefficient of Thermal Expansion (α x 10^{-} K^{-1})
	a (Å)	c (Å)	a (Å)	c (Å)	
AISI-304	3.58	-	3.59 [74]	-	17.3 [75]
TiO_2	3.78	9.47	3.79 [76]	9.51 [76]	7.8 [77]
FTO	4.73	3.20	4.74 [78]	3.19 [78]	3.5 [79]
SiO_2	-	-	4.91 [80]	5.41 [80]	0.55 - 0.75 [80]
Al_2O_3	-	-	4.79 [81]	12.99 [81]	4.5 - 10.9 [81]
MgO	-	-	4.21 [82]	-	9 – 12 [82]

4.3 AFM INVESTIGATIONS

In order to understand the topography of the films that were prepared, atomic force microscopy (AFM) was used. Since the particulate morphology of SiO_2, Al_2O_3 and MgO could be problematic for AFM cantilever, only TiO_2 and FTO coated samples were investigated with this technique. As seen in **Figure 4.22**, the surface morphology of TiO_2 coated SS substrate was neat. No particulates or undesired topographic features were observed due to both surface roughness and cleanliness of the substrate and growth of TiO_2 film on the surface. The average roughness values were also calculated. For TiO_2 coating, the average roughness values were found as Ra = 8.83 nm and Rq = 11.13 nm, where Ra and Rq represents arithmetic and root mean square

of the roughness calculated. The application of FTO coating on TiO_2, carries the topographic behavior of TiO_2 layer below as expected, shown in **Figure 4.23**. The scale in the figure represents the height of the measured area where light areas have larger height. Calculating the average roughness of FTO film resulted as Ra = 16.22 nm and Rq = 24.28 nm.

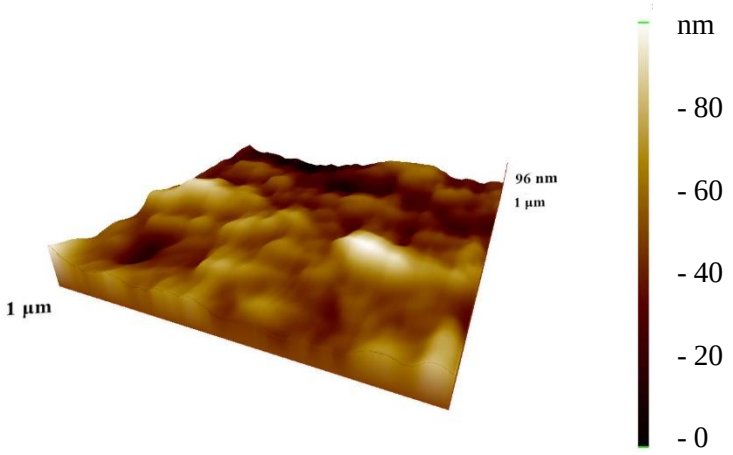

Figure 4.22 3D AFM image of TiO_2 coated AISI 304 SS (TiO_2 thickness of ~650 nm) prepared by USP.

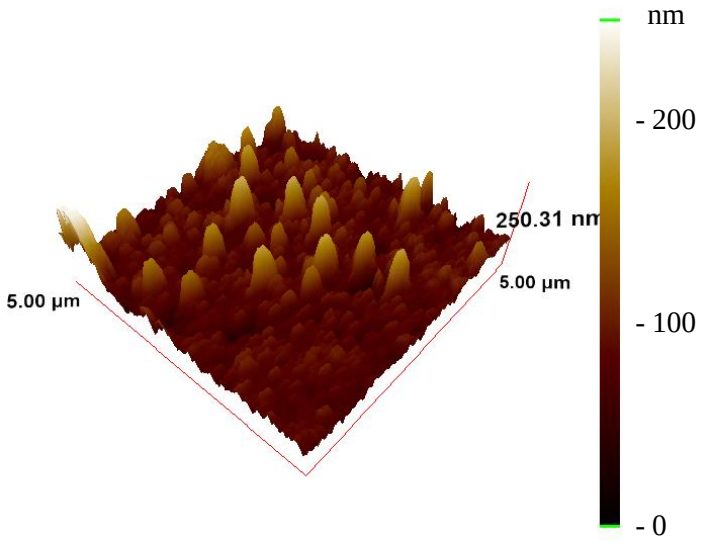

Figure 4.23 3D AFM image of FTO coated AISI 304 SS with TiO_2 intermediate layer (total thickness of ~1 µm) prepared by USP.

Looking at the phase image on the left-hand-side of **Figure 4.24**, complete coverage of FTO layer above TiO_2 layer was clearly observed. Also, the histogram on the right-hand-side shows that homogeneous film was obtained and its histogram is within a close fit to normal distribution. Although there are some rod-like surface features observed during the AFM investigation, they were not completely distributed throughout the surface but rather at some local points. The reason for this type of growth may be caused by the USP technique in which some larger particles exist in the mist. The AFM image given in **Figure 4.23** was deliberately taken from an area which showed both rod-like growth (upper parts) and normal growth (lower parts) in order to explain particle-related technicalities. In order to prevent this issue, a filter can be used that selectively eliminates large particles having undesired size that were generated and send those particles back to the ultrasonic chamber. Particle filtration can increase the quality of the films further.

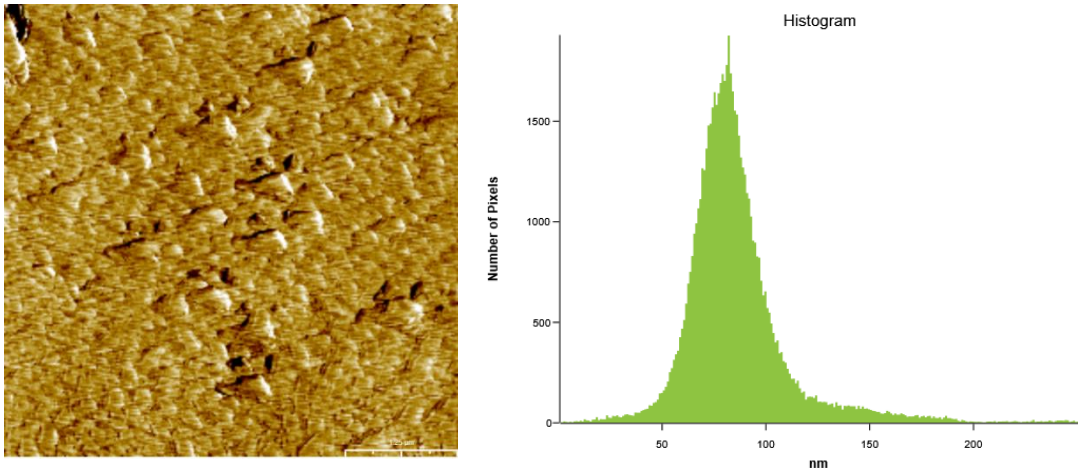

Figure 4.24 (left) Phase image of FTO coated AISI 304 SS with TiO_2 intermediate layer (total thickness of ~1 μm for FTO and TiO_2) and (right) histogram of the measured area.

4.4 BREAKDOWN VOLTAGE (BDV) MEASUREMENTS

Breakdown voltage (BDV) measurements were conducted, without thermocouple contact, at room temperature. The voltage was applied for a short time (<1 s) in order to disregard the effect of electron "avalanche" that cause the breakdown. There are

several material properties that affect BDV. The contacts on the sample surface were fixed so that every measurement would correspond to the same local point.

As seen in **Figure 4.25**, all of the samples showed a close-to-linear voltage-current relationship which was formulized as V = IR. However, after a certain applied voltage, the current suddenly jumps to higher values and reaches the maximum current output of the device. When the current jumps to these values, it showed that the current no longer flows through the coating but rather from the underlying stainless steel substrate. This means that the coating is electrically broken down. The sudden jump of the current, therefore, can be considered as the BDV value of the material under these conditions. Remaining coatings of insulating layers, SiO_2, MgO and Al_2O_3, showed almost no resistance against breakdown due to absence of any insulating layer formed and failed below 5V of applied voltage. FTO, on the other hand, due to the loading condition (significantly larger current flow) electrically broke down after 5V.

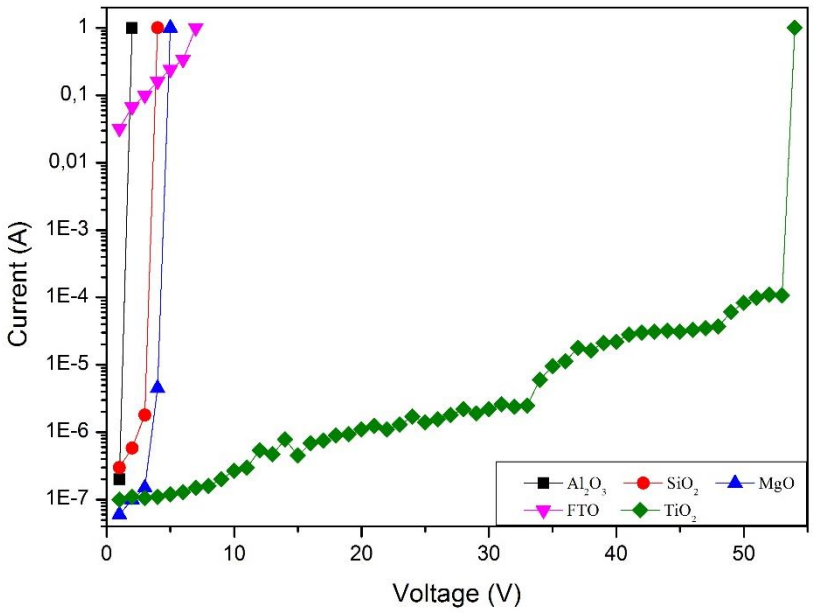

Figure 4.25 Current (A) vs voltage (V) plot of the coated films on AISI 304 stainless steel substrate prepared by USP.

Carrying much larger electron concentration under this loading conditions (average around 0.2 A), ultimately effects the BDV value of FTO layer alone. After applying more than 6 V, FTO layer cannot carry the electron flow anymore, and current starts

to flow from the underlying SS substrate. Therefore, it is essential to isolate FTO layer from the conductive substrate (in this case, SS) if the loading condition is planned to be above 6 V. Considering TiO_2 it can withstand over 50 V of applied voltage. However, due to local heating caused by high voltage applied which generates a small amount of current flow in the order of 10^{-3} A, after a certain voltage value there was a sudden current increase which corresponds to 54 V. Although it seems that TiO_2 can withstand to 54 V of applied voltage, one should keep in mind that the loading condition would change when FTO layer is applied on top of this TiO_2 layer. Both increase in temperature and current flow density would affect its BDV value, hence one should not expect to work around close to 54 V of applied voltage.

Thickness dependency of BDV for TiO_2 was also investigated. Five different samples were prepared for this purpose by altering the spray-cycle. Applying the same method for determining BDV values, **Figure 4.26** was obtained. As seen from the figure, as the thickness of TiO_2 layer increases, so does the BDV value, as expected. The corresponding BDV values for these coatings 3 V, 6 V, 12 V, 25 V and 54 V for T1, T2, T3, T4 and T5, respectively.

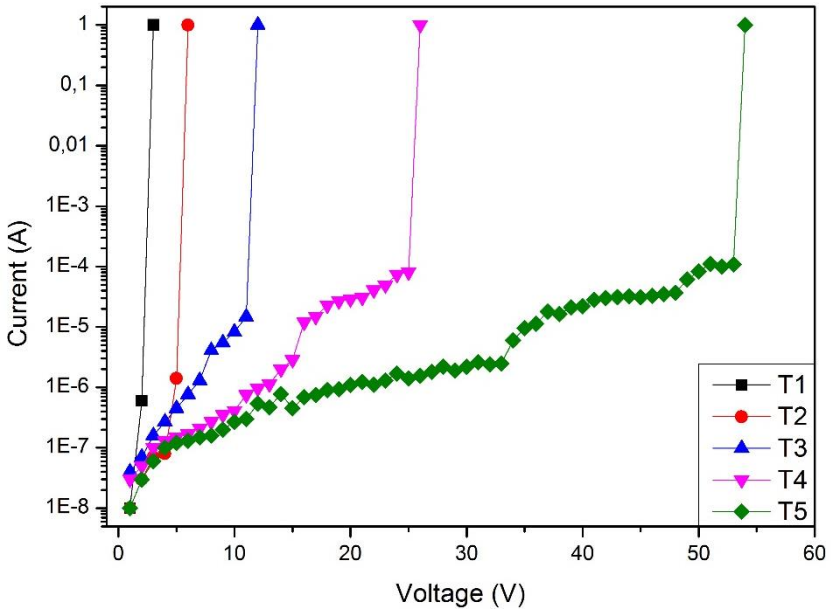

Figure 4.26 Current (A) vs voltage (V) plot of TiO_2 coated films on AISI 304 stainless steel substrate prepared by USP with three different thickness values for T1 (~85 nm), T2 (~130 nm), T3 (~170 nm), T4 (~270 nm) and T5 (~650 nm).

As seen from **Figure 4.27**, the relationship between BDV and TiO_2 thickness was obtained. The average increase of BDV per unit thickness (nm) can be calculated which was found to be around 0.087 V/nm or 87 V/μm for TiO_2 layer. Obtaining thicker layer would increase the BDV, however, the growth of TiO_2 after a certain thickness value yields particulated or agglomerated morphology on the substrate surface.

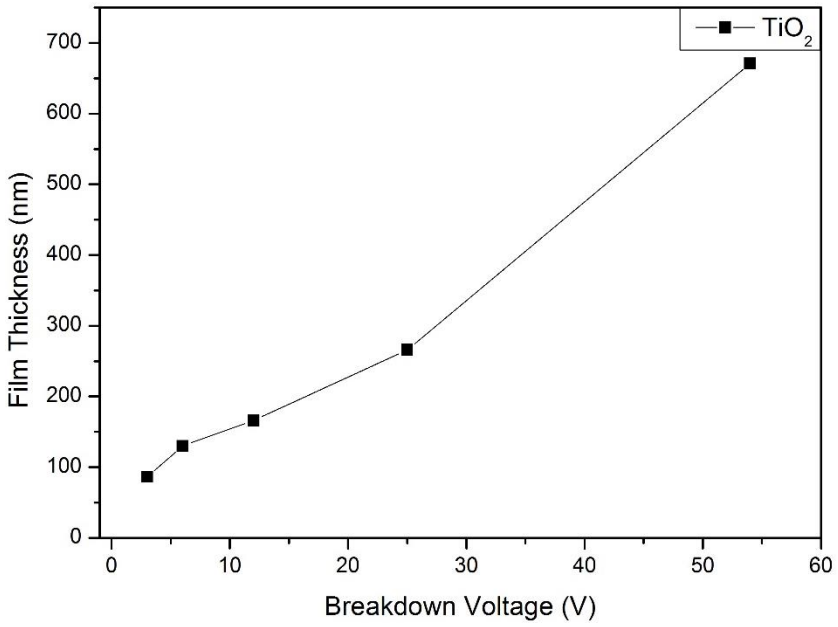

Figure 4.27 Film thickness (nm) vs BDV (V) plot of TiO_2 coated AISI 304 SS samples with different thickness values prepared by USP.

The temperature dependency of BDV was also investigated. For this purpose, the samples were placed on a heater-plate. The temperature range for the measurement was held from room temperature (25 ^oC) to 400 ^oC. Current (A) vs voltage (V) graph was plotted accordingly, as seen from **Figure 4.28** and **Figure 4.29**. The samples were heated until a desired temperature was reached, measured from the thermocouple attached on the substrate and controlled in every step. Once the temperature has become constant, the measurement of BDV was conducted in a similar manner explained before. The individual lines represented in **Figure 4.28** show the temperature at which the measurement was done. As seen from the figure, when temperature increases there is a decrease in the BDV values.

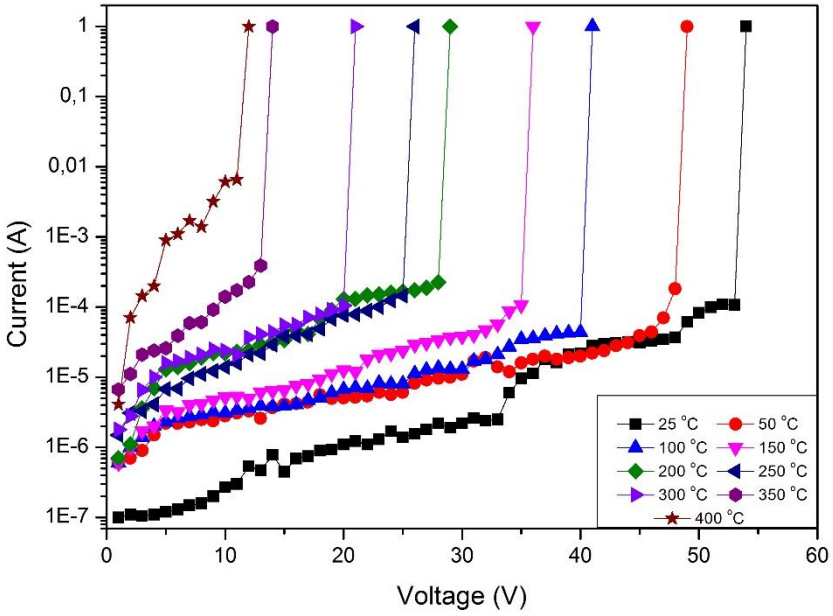

Figure 4.28 Current (A) vs voltage (V) plot of TiO_2 coated AISI 304 SS sample (T5) measured at different temperatures from room temperature to 400 ºC.

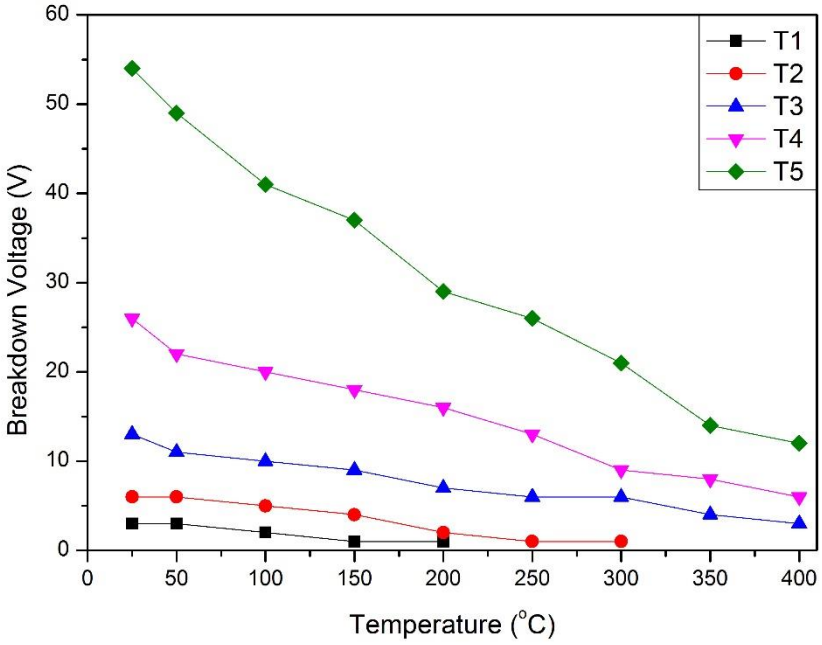

Figure 4.29 Breakdown voltage (V) vs temperature (ºC) plot of TiO_2 coated AISI 304 SS samples prepared by USP.

Even though the figure seems a bit complex, it is essential to understand the temperature dependency of BDV of the samples. Hence, more simple graph was

plotted which summarizes the temperature effect. **Figure 4.29** strongly suggests that the temperature is a major factor that affects BDV of the samples. The temperature dependency of the samples having five different thickness values was observed with slight deviations from a linear fit. Note that, for T1 and T2, after a certain temperature the sample immediately conducts electricity to the underlying stainless steel substrate even under 1 V of applied voltage which was found to be around 150 ^{o}C and 250 ^{o}C, respectively.

The temperature and thickness dependencies of the TiO_2 coated samples (T1-T5) including individual film thickness values were given in **Table 4.4**. The temperature dependency of the coatings increases with coating thickness which indicates that TiO_2 films with greater thickness are more sensitive to temperature. However, looking at the thickness dependency of these films, one can conclude that the contribution of thickness to BDV of the samples seems limited and maximized for T4. The increase of BDV per unit thickness tends to decrease after a certain thickness value.

Table 4.4 Characteristics of the BDV experiments including temperature and thickness dependencies with individual film thickness values for T1-T5 prepared by USP.

Sample Label	Thickness (nm)	BDV at Room T. (V)	BDV at 400 ^{o}C (V)	Temperature sensitivity of BDV (V/^{o}C)	Thickness sensitivity of BDV (V/μm)
T1	85 ± 35	3	<1	- 0.016	34.7
T2	130 ± 25	6	<1	- 0.022	46.1
T3	165 ± 10	12	3	- 0.024	72.3
T4	265 ± 25	25	6	- 0.051	94.1
T5	670 ± 15	54	12	- 0.112	80.4

4.5 SHEET RESISTANCE MEASUREMENTS

Sheet resistance (R_{sh}) values are important for thin films to determine the electrical properties of the obtained films. R_{sh} values of the produced FTO layers were measured using JANDEL universal probe. It is essential to understand these values which determine the resistivity of the coating. The obtained results would alter the heating experiments since lower the resistance higher the current which would yield different saturation temperatures during heating experiments because of the current dependency of the generated heat. Different sheet resistance values were obtained for FTO films, as shown in **Table 4.5**. However, having highly conductive FTO layer was not logical since the current flow was not enough to generate enough heat due to the coating having less resistance against the flow. The resistivity values of the films can be obtained by multiplying sheet resistance with film thickness. Using this relationship, dependency of resistivity for FTO layers on F/Sn ratio can be found, as shown in **Figure 4.30**.

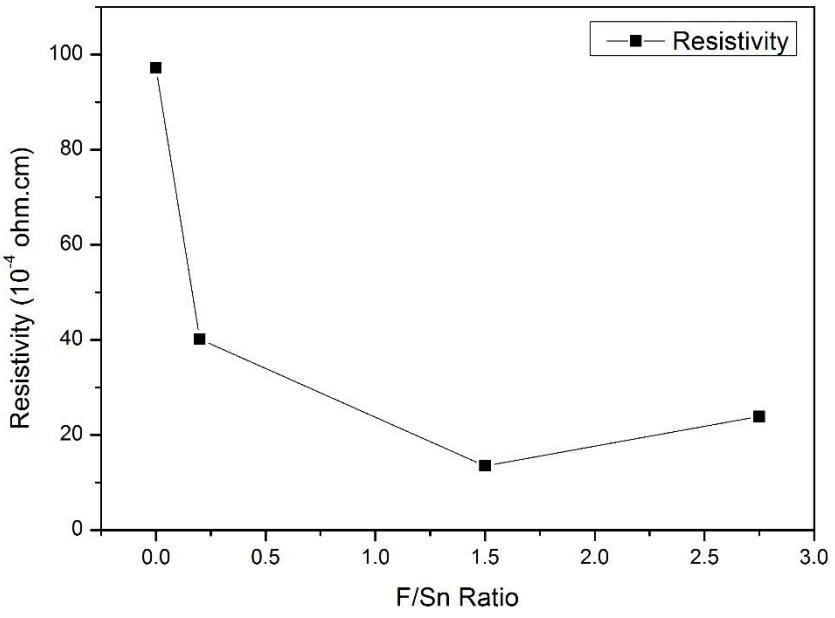

Figure 4.30 Resistivity dependency of FTO films on F/Sn ratio prepared by USP.

As seen from the plot, resistivity values decrease with respect to increase in F/Sn ratio. However, after reaching F/Sn ratio of 1.5, the resistivity values start to increase again. This is simply due to the fact that, beyond this critical value, it is no longer possible for ionic substitution of F^- with O^{-2} which corresponds to solubility limit of F^- in SnO_2 lattice.

Table 4.5 The properties of the samples (TF1-TF6) including sheet resistance (Ω/□), and resistance between bus bars (Ω.cm) with individual TiO_2 and FTO thickness values.

Sample Label	Thickness (nm)		Bus bar Resistance (Ω.cm)	Sheet Resistance (Ω/□)	F/Sn Ratio (At.)	Resistivity ($\rho \times 10^{-4}$ Ω.cm)
	TiO_2	FTO				
TF1	660 ± 25	160 ± 20	12.8	67.8 ± 2.3	1.5	10.9
TF2	660 ± 60	350 ± 40	2.5	46.0 ± 1.6	1.5	16.1
TF3	600 ± 30	310 ± 30	45.4	130.1 ± 9.8	0.2	40.2
TF4	770 ± 20	150 ± 10	240.1	690.6 ± 72.0	0	102.5
TF5	620 ± 20	260 ± 15	130.6	361.3 ± 2.7	0	91.9
TF6	660 ± 25	160 ± 20	27.8	122.4 ± 11.8	2.7	23.9

Also, a decrease in the sheet resistance values were observed as thickness of the films increases. However, after a certain thickness value, cracking of the film and/or particulate growth occurred during deposition process. Therefore, there is a practical limit for FTO growth which made it not practical to lower the sheet resistance values any further. Only five samples (TF1-TF5) were selected for further heating experiments.

4.6 HEATING EXPERIMENTS

Heating experiments were carried out as explained in Chapter 3.4. The temperature and current data were recorded for every 10 s and plotted accordingly. The FTO coated samples, both with and without intermediate TiO_2 layer, were compared with commercially available bare AISI 304 SS substrates used in this work. As seen from **Figure 4.31**, 3.2 A of current flow across the silver pastes generated sufficient electrical current for the SS substrate to reach ~130 ^{o}C in approximately 6 min. The resistance of SS was not high enough to efficiently convert electrical energy into heat. Also, since the thickness of the substrate is 2 mm, the cross-sectional area of the substrate is high enough to easily carry the electrical current through contacts which barely elevates the temperature of the sample to 130 ^{o}C from room temperature.

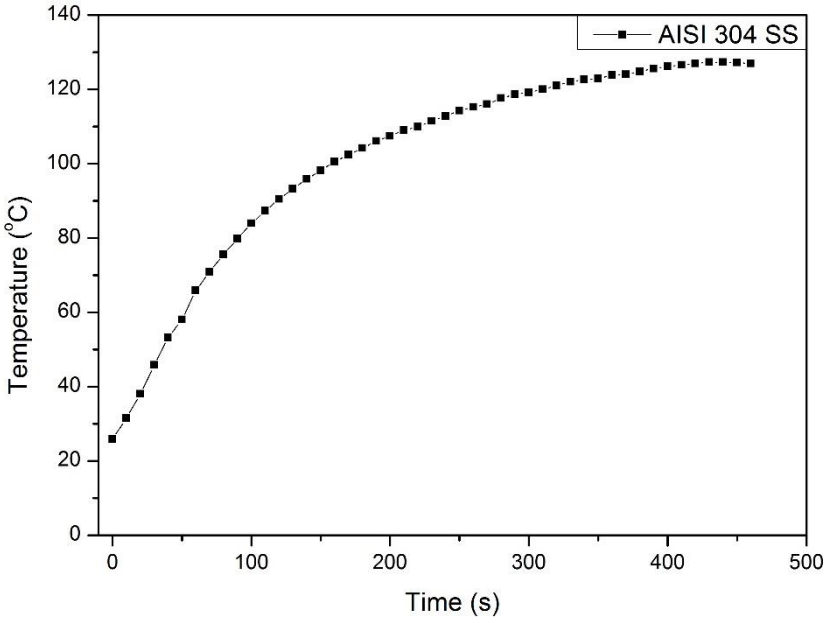

Figure 4.31 Heating curve of bare AISI 304 stainless steel substrate (2 mm in thickness) under 12 V applied voltage.

When FTO coated SS with TiO_2 intermediate layer is considered, as seen in **Figure 4.32**, it was possible to reach above 300 ^oC with 5 V of applied voltage. The reason of not having gradual increase in the temperature with increased voltage is simply that the current flow across the coating is cumulatively increasing with temperature. Higher temperatures yield higher current flows which again provide higher temperatures. Under 3 V of applied voltage, on the other hand, the temperature increase of the substrate was not sufficient to provide higher electrical current. Hence the resulting temperature, even after 10 min, was not sufficient. After applying 5 V, this loop-like increase of both temperature and electrical current was possible, hence the sudden increase of the temperature was observed. However, applying higher voltages than 5 V was not meaningful since the current limit (3.2 A) was already reached and the temperature increases were similar for 7 V, 10 V and 12 V. The saturation temperature for this sample was found to be around 330 ^oC. The results showed that this sample is convenient and suitable for achieving high temperatures with less than 5 V of applied voltage.

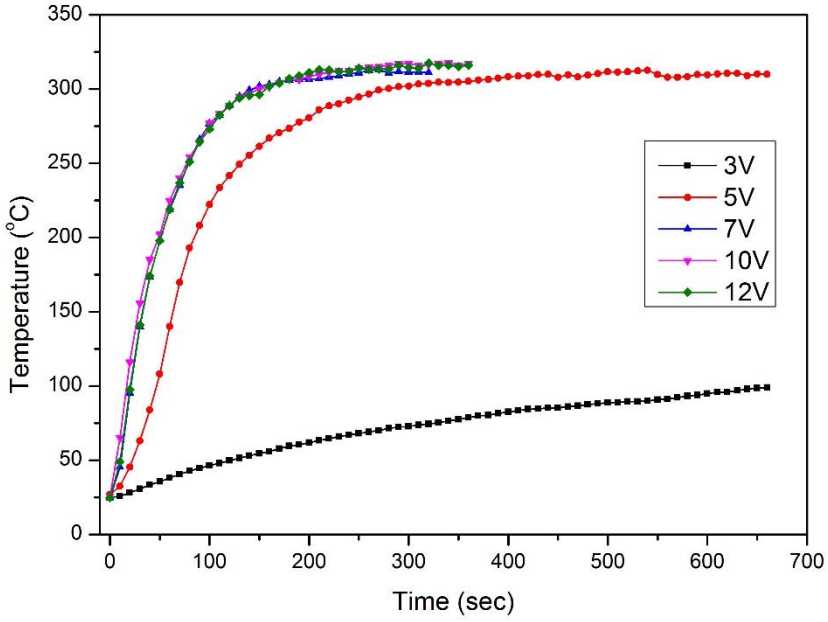

Figure 4.32 Heating curve of sample TF1 under various applied voltages.

Since the bus bar resistance across the silver pastes were smaller for TF2 compared to TF1, the generated currents were similar for 3 V, 5 V, 7 V and 10 V. Hence, the resulting temperatures obtained for the sample TF2 were similar with each other, indicating that the saturation temperature was around 230 ^{o}C, shown in **Figure 4.33**. As expected, more conductive coating generates less resistance for electron flow, which results in a lower saturation temperature. Hence, as the results indicate, the saturation temperature is lower than TF1, which makes the sample TF2 still suitable for heating purposes. However, due to TF2's higher electrical conductivity compared to TF1, the saturation temperature was reached in longer period which clearly indicates that its efficiency is much less.

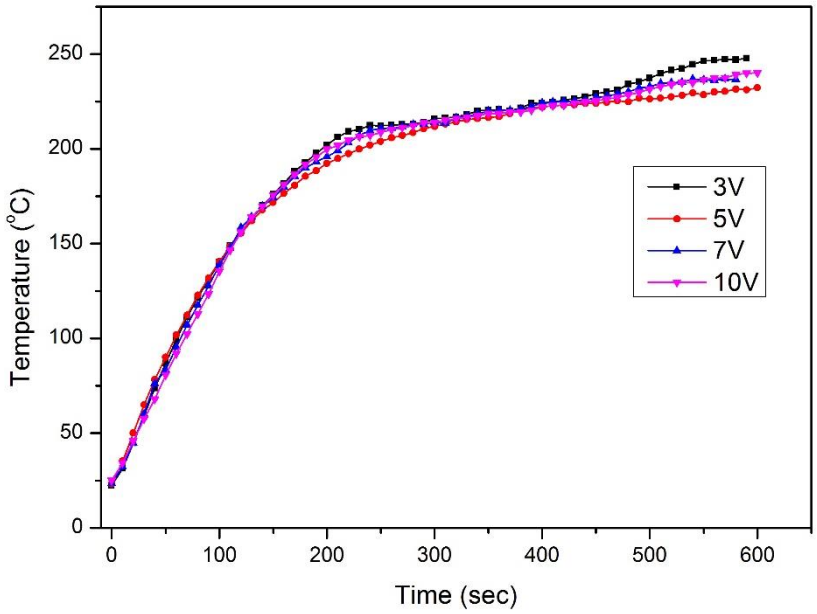

Figure 4.33 Heating curve of sample TF2 under various applied voltages.

Considering the more resistive sample (TF3), it reached close to 200 ^{o}C under 5 min with 5 V. However, when applied voltage was 12 V, the temperature increase was really sharp and reached to 280 ^{o}C under 2 min. Although the temperature reached was satisfactory, the electrical breakdown occurred after certain temperature and current flow as seen from **Figure 4.34**. Hence, the sample started to cool down since the current started to flow from SS which shows much less resistance against the flow. Since the TiO_2 coating was thinner compared to TF1 and TF2, the FTO layer could not carry the electrical load any longer, including TiO_2 intermediate layer, hence the

breakdown occurred. A similar problem occurred in TF4 as well. Since TF4 was more resistive compared to TF3, electrical current response with increasing temperature was late in a similar manner. Once the current flow started to develop and was high enough, the temperature started to increase rapidly. However, similar to TF3, after a certain temperature the electrical breakdown occurred and temperature started to decrease. Due to these electrical breakdown related problems, TF3 and TF4 are not suitable for heating purposes, especially under high applied voltages.

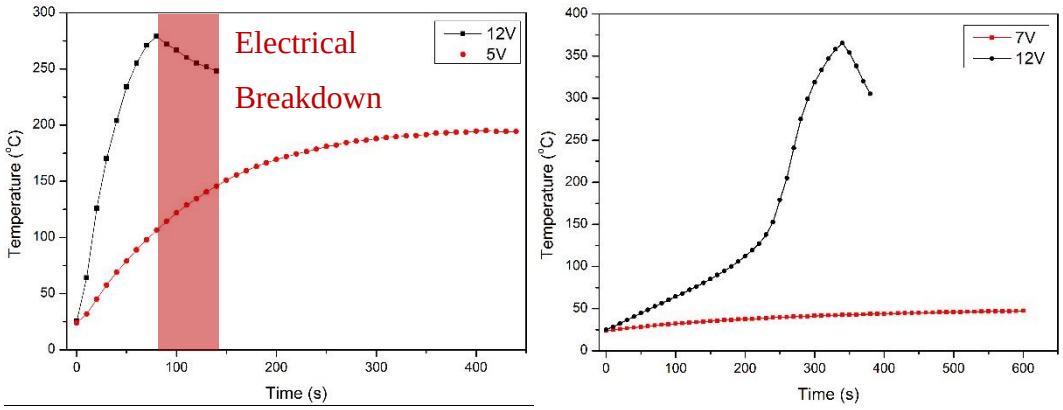

Figure 4.34 Heating curve of samples TF3 and TF4 under various applied voltages.

The thickness of FTO layer for sample TF5 was larger than sample TF4, hence it could withstand the applied voltage even at increased temperatures as seen in **Figure 4.35**.

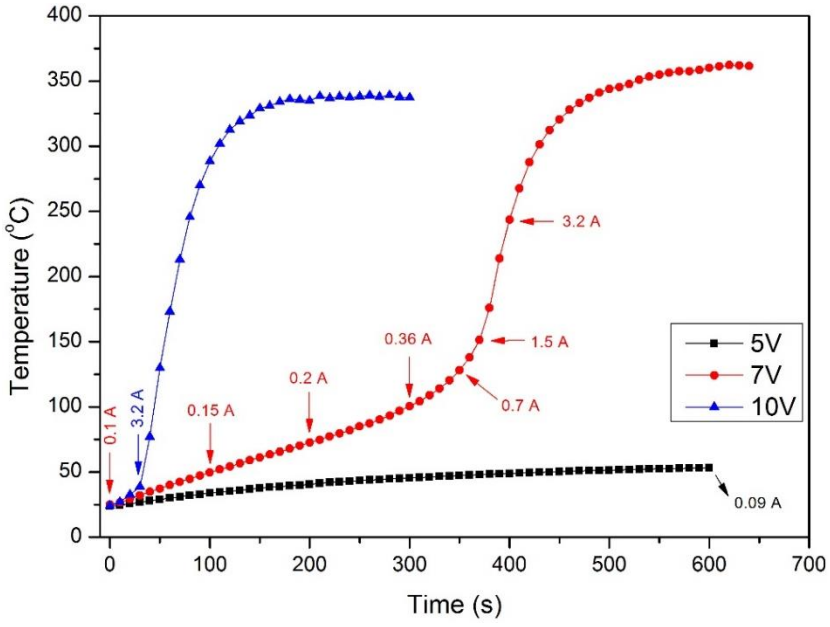

Figure 4.35 Heating curve of sample TF5 under various applied voltages.

Even though 7 V was lagged to reach higher temperatures because of the slow development of the electrical current, 10 V was sufficient to rapidly increase the temperature close to 350 ^{o}C without any occurrence of electrical breakdown, indicating that the coating thickness was sufficiently high to support these loading conditions. However, due to TF5's high electrical resistivity, the temperature response of the current flow was delayed. Therefore, one can conclude that, although the sample did not electrically breakdown, it is not quite effective for heating applications, especially when low applied voltages are considered.In order to understand the repeatability of the heating and cooling of the samples, cyclic heating experiments were conducted. Sufficient time was provided to the test setup so that cooling to room temperature was ensured during the experiments. For this purpose, the sample that showed the best performance during heating experiments was selected among all which was TF1. The results of the cyclic heating experiments for the best sample (TF1) can be seen in **Figure 4.36**.

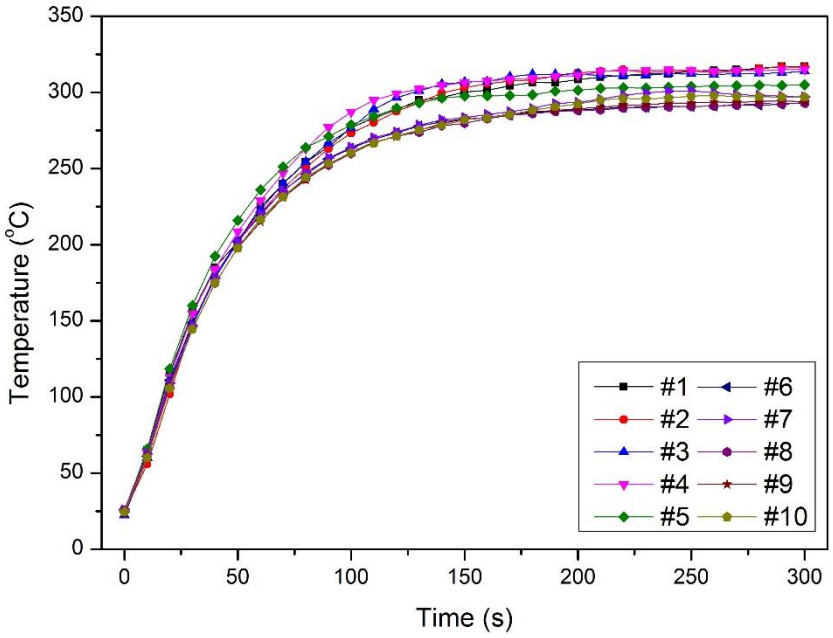

Figure 4.36 Cyclic heating experiments for sample TF1 under the same applied voltage of 10 V with total number of 10 cycles.

As compared to the initial heating experiments, there exists a slight decrease in the saturation temperature of the samples. This can be explained by the annealing of the sample during heating experiments. Most of the studies reported that post-annealing

of the FTO layers after deposition further lowers the resistivity of the coating [23,83,84]. Since the heating experiments were conducted under laboratory conditions, the experiments may have provided sufficiently high temperature and duration similar to annealing conditions. Therefore, a slight decrease in the temperature was observed.

In order to understand the annealing-related issue mentioned above, another set of cyclic (10 cycles) experiments were conducted to the same sample (TF1). The voltage difference across the bus bars were also recorded as seen in **Figure 4.37**.

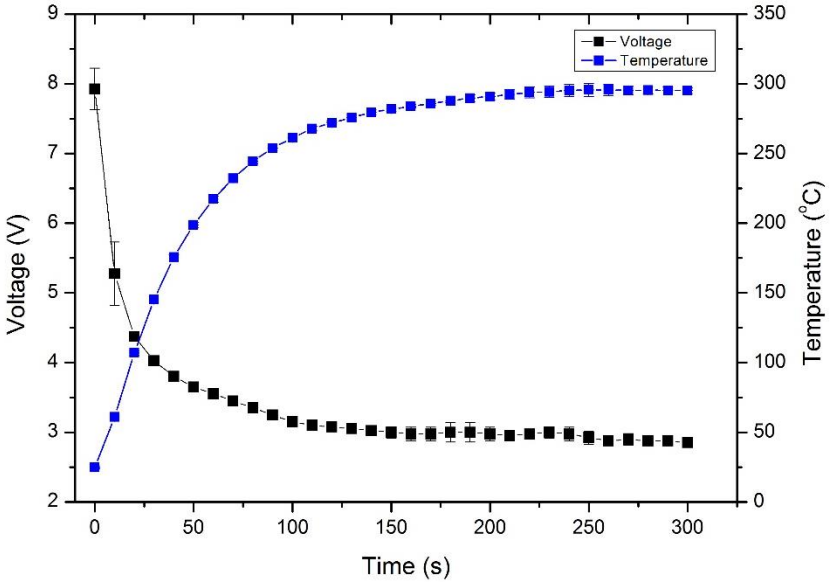

Figure 4.37 Re-cyclic heating experiments for sample TF1 under the same applied voltage of 10 V prepared by USP.

The corresponding voltage measured across the bus bars was decreasing with increasing temperature. The decrease in the resistance of the sample due to increase in temperature, made it possible to supply maximum current of 3.2 A with lower voltages, accordingly. The saturation temperature was reached around 300 ^{o}C with corresponding voltage of 2.9 V and 3.2 A of current. The saturation temperature deviation was almost negligible after re-cyclic tests were conducted. The electrical properties of the sample were no longer affected by re-cyclic heating experiments. The deviance of the temperature during experiments, even though it is very small, can be explained by the change in the laboratory conditions such as the ambient temperature

and humidity. After the stabilization of re-cyclic heating experiments, the saturation temperature can said to be constant at ~300 ^{o}C with corresponding current flow of 3.2 A for sample TF1. The properties of the samples after BDV measurements and heating experiments, including energy input, output and efficiency calculations are given in **Table 4.6**.

Table 4.6 The properties of the samples after BDV measurements and heating experiments including power (output and input) and efficiency calculations, accordingly.

Sample	**Thickness (nm)**		**BDV (V)**	**R_{sh} (Ω/□)**	**T_f (^{o}C)**	**t_f (s)**	**Energy (kJ)**		**Eff. (%)**
	TiO_2	**FTO**					**Output**	**Input**	
AISI-304	-	-	-	-	127	420	0.2	2.7	**7.3**
T1	85 ± 35	-	3	-	-	-	-	-	-
T2	130 ± 25	-	6	-	-	-	-	-	-
T3	165 ± 10	-	12	-	-	-	-	-	-
T4	265 ± 25	-	25	-	-	-	-	-	-
T5	670 ± 15	-	54	-	-	-	-	-	-
TF1	660 ± 25	160 ± 20	-	67.8 ± 2.3	315	260	0.6	2.0	**28.6**
TF2	660 ± 60	350 ± 40	-	46.0 ± 1.6	235	500	0.4	2.7	**15.7**
TF3	600 ± 30	310 ± 30	-	130.1 ± 9.8	X	-	-	-	-
TF4	770 ± 20	150 ± 10	-	690.6 ± 72.0	X	-	-	-	-
TF5	620 ± 20	260 ± 15	-	361.3 ± 2.7	340	260	0.5	2.2	**23.4**

T_f represents the saturation temperature attained in time, t_f (s). Energy output, input (kJ) and efficiency (%) calculations were done according to the equations (2.1), (2.2), (2.3), (2.4) and (2.5) given in Chapter 2.3. The calculations could not be done for TF3 and TF4 because they electrically breakdown during heating experiments. The failure of TF3 might be due to a thinner TiO_2 layer formed compared to other samples. For TF4, on the other hand, the problem might be caused by the FTO layer. Since the FTO layer for this sample is very thin (150 nm), the avalanche effect of electrical breakdown might have taken place. However, the efficiency calculations for the remaining samples (TF1, TF2 and TF5) including bare AISI-304 SS, showed remarkable difference. Efficiency value of bare AISI-304 SS indicates that the electrical energy input was converted to heat by a factor of only 7.3%. On the other hand, the FTO coated samples with TiO_2 intermediate layer, even the least efficient sample (TF2) yielded twice as much efficiency compared to bare AISI-304 SS. Highest efficiency was obtained for sample TF1, reaching almost 30%. Achieving higher efficiency was not the only challenge in this work, but also to reach high temperatures. AISI-304 SS reached to 127 ^oC after a long period of time, around 420 s, whereas a higher temperature of 320 ^oC was reached with shorter amount of time, for sample TF1.

Also, the results from Hall-Effect measurements were tabulated and given in **Table 4.7**. The growth rates were calculated by measuring the coating thickness revealed through SEM investigations divided by the time elapsed during deposition. Carrier mobility values are one of the main factors determining the electrical conductivity of a material. As seen from the table, when F/Sn ratio increases, the mobility of the electrons decreases. This can be explained by the fact the increase in the amount of dopant, inevitably affects their mobility by introducing higher probability of scattering events. The resistivity values, as expected, increased by decreased F/Sn ratio. Decreasing the F^- doping amount also decreases the number of free electrons provided to the system, hence it becomes more resistive.

Table 4.7 Various parameters of FTO coatings with intermediate TiO_2 layers produced by USP.

Sample	Thickness (nm)		Growth Rate (nm/min)		F/Sn Ratio (At.)	Mobility (cm^2/Vs)	R_{sh} ($\Omega/\square$)	Resistivity ($\rho \times 10^{-4}$ $\Omega.cm$)
	TiO_2	FTO	TiO_2	FTO				
TF2	660 ± 60	350 ± 40	40.3	106.0	1.5	9.4	46.0 ± 1.6	16.1
TF3	600 ± 30	310 ± 30	36.1	103.2	0.2	58.9	130.1 ± 9.8	40.2
TF4	770 ± 20	150 ± 10	46.5	91.1	0	72.6	690.6 ± 72.0	102.5

All of these results show that, especially for flat surface heating designs, conducting thin films of FTO layers with intermediate TiO_2 layers, to overcome electrical breakdown, can be used. Having higher efficiency in energy conversion makes them suitable and candidate materials to replace commercial heaters.

4.7 HUMIDITY TEST

Due to the fact that the humidity tests are destructive, these tests were carried out after completion of all heating experiments. The test is composed of five cycles (2 days each) with total of 10 days. The temperature range was 20-60 ^oC and 95% relative humidity was sustained during the test without any interruptions. The test conducted is almost similar to MIL-STD-810G (American Department of Defense Test Method Standard: Environmental Engineering Considerations and Laboratory Tests) [85]. The results of the humidity test can be seen in **Figure 4.38**.

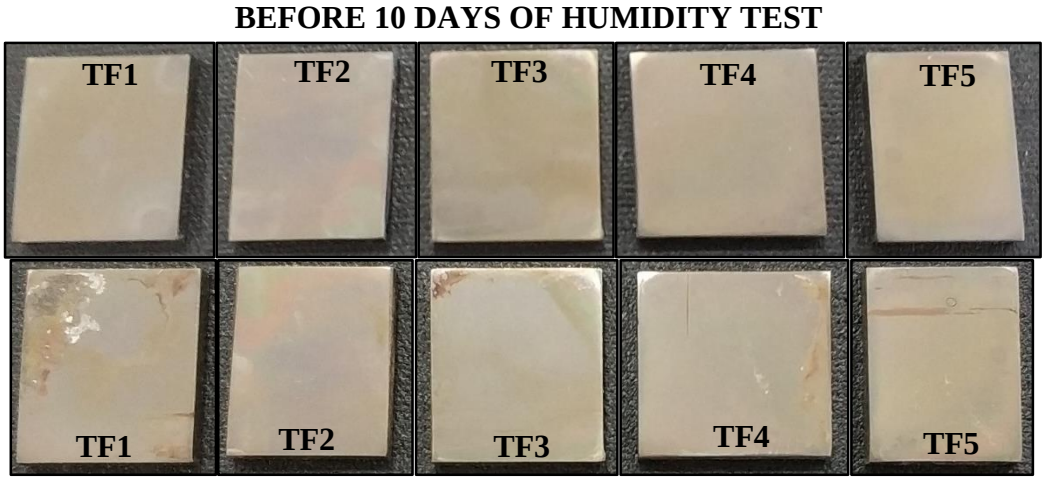

Figure 4.38 Samples (TF1-TF5) before and after 10 days of humidity test under 95% relative humidity conditions.

Among the samples, generation of degraded edge can be observed for sample TF1 while others were hardly degraded. The reason of localized degradation for sample TF1 might be correlated with the presence of a thin layer of FTO coating above the TiO_2 intermediate layer. Although the degraded areas can be observed due to edge effect during the test, the middle areas of the samples are still conductive and did not degrade or fail. For that purpose, sheet resistance measurements were conducted again for these samples. The results for the sheet resistance values, resistivity values and change in resistivity before and after the humidity test were summarized and given in **Table 4.8**. The results indicated that the FTO layer is rather resistant against humid environments which proves its usability for a long period of time under moist environmental conditions. Also, the overall change of resistivity (%) remained below 5% for each sample according to equation (4.4):

$$Percent\ Resistivity\ Change = \frac{|\rho_2 - \rho_1|}{\rho_1}\ x\ 100 \qquad \text{[Eq. 4.4]}$$

where ρ_1 and ρ_2 represents resistivity before and after humidity test, respectively.

Table 4.8 Sheet resistance (R_{sh}) and resistivity values of the samples prepared by USP (TF1-TF5) before and after humidity tests.

Sample	Thickness (nm)		Before Humidity Test		After Humidity Test		Resistivity Change (%)
	TiO_2	FTO	R_{sh} (Ω/□)	Resistivity ($\rho \times 10^{-4}$ Ω.cm)	R_{sh} (Ω/□)	Resistivity ($\rho \times 10^{-4}$ Ω.cm)	
TF1	660 ± 25	160 ± 20	67.8 ± 2.3	10.9	66.9 ± 2.3	10.7	1.8
TF2	660 ± 60	350 ± 40	46.0 ± 1.6	16.1	44.2 ± 4.3	15.5	3.7
TF3	600 ± 30	310 ± 30	130.1 ± 9.8	40.2	130.6 ± 11.0	40.5	0.7
TF4	770 ± 20	150 ± 10	690.6 ± 72.0	102.5	711.7 ± 69.3	106.8	4.2
TF5	620 ± 20	260 ± 15	361.3 ± 2.7	91.9	371.1 ± 9.0	96.5	5.0

Having less than 5% resistivity change is an indication that FTO coatings are highly stable under such environmental conditions without degrading or failing.

CHAPTER 5

SUMMARY AND CONCLUSIONS

In this study, the production and development of FTO coated AISI 304 stainless steel substrates including insulating oxide layers sandwiched in between was accomplished using ultrasonic spray pyrolysis technique for heating applications. The possible problem that could arise from passing electrical current through FTO layer when there exists a more conductive material beneath was electrical breakdown, which is simply the shift of current flow from less resistive material when a certain amount of voltage is reached that is defined as the breakdown voltage of the material. In order to overcome this problem, an insulating layer has to be integrated in between FTO layer and the substrate.

There were four different candidates for insulating oxide layers: magnesium oxide, MgO, silicon dioxide, SiO_2, aluminum oxide, Al_2O_3 and titanium dioxide, TiO_2. All of these layers were deposited on pre-polished 304-SS substrates using ultrasonic spray pyrolysis (USP) method. The deposition conditions and parameters were kept constant for each having substrate temperature of 500 ^oC, 4.5 cm nozzle-to-substrate distance, solution molarity of 0.1 M with corresponding weight of the precursor dissolved in methanol. Only exception was TiO_2, since titanium iso-propoxide does not dissolve in methanol but in iso-propanol, the precursor was mixed with both solvents with a ratio of 1:1 so that both dissolution and mist generation was successful. It was necessary to use methanol-based solutions in the ultrasonic chamber since the power was not sufficient to break the bonds of iso-propanol-based solutions. After overcoming this problem, each sample was investigated using scanning electron microscopy (SEM) in order to observe the coating thickness and morphology above the substrate surface. However, among all the candidate oxide layers, only TiO_2 layer

was successfully grown as a continuous and homogeneous layer on the substrate surface under given process parameters. This may be due to temperature or precursors used for the deposition. Both temperature but mainly the precursor itself changes the wetting environment drastically, which inevitably affects the growth of the film above the surface. Changing process parameters enabled to obtain various coating thicknesses. However, there exists an upper limit to film growth in which when a certain thickness is reached, the particles tend to agglomerate and form particulates above the substrate surface. Despite this, a homogeneous TiO_2 layer of ~700 nm thickness was successfully deposited on AISI 304 stainless steel substrate using USP at 500 ^oC.

Also, FTO was coated on bare 304-SS in order to observe the behavior of it under the applied voltage. It was found that 5V of applied voltage at room temperature was enough for electrical breakdown of FTO layer which limits its usage. It was already discussed that breakdown voltage is quite sensitive to temperature increase which further restricts the use of FTO coating without introducing any insulating layer in between. Using secondary electron imaging through SEM was not sufficient to distinguish individual layers of TiO_2 and FTO because they showed very similar contrast and was almost indistinguishable. Therefore, back-scatter mode of SEM was used to observe the thickness values of the layers separately. Also, with the help of EDS-mapping, the existence of both layers were successfully proven.

Although the intermediate oxide layers other than TiO_2 were not continuous, they were still investigated for their breakdown voltage (BDV) values. BDV values found for each individual layer were 2 V, 4 V, 5 V, 6 V and 54 V for Al_2O_3, SiO_2, MgO, FTO and TiO_2, respectively. It was clear that TiO_2 shows remarkable performance compared to other oxide layers which made it the best candidate for this purpose. Also, in order to investigate the thickness dependency of BDV, five different TiO_2 coated samples with various thickness values were investigated. As expected, the BDV values were found to be increasing with increasing thickness. The thickness values were found to be between 85-670 nm with corresponding BDV values of 3-54 V. Besides the thickness, the temperature dependence of BDV for TiO_2 layers was also

investigated. The experiments showed that there was an inverse relationship between BDV and temperature.

To conduct heating experiments, FTO layer was deposited on top of TiO_2 coated 304-SS samples. The deposition parameters were kept the same and TiO_2 layer having highest thickness (sample T5) was selected as the intermediate layer since it would, obviously, show the best result. Therefore, five different FTO layers were deposited having different resistance values between applied silver paste of bus bars: TF1 (12.8 Ω.cm), TF2 (2.5 Ω.cm), TF3 (45 Ω.cm), TF4 (240 Ω.cm) and TF5 (130 Ω.cm). It is expected that the sample with lower resistance would draw higher current which would yield much higher saturation temperature due to Joule's law of heating. Also, TF3 and TF4 were observed to undergo electrical breakdown during the experiments since both temperature increase was too sharp and electrical current density developed was too large to carry by these samples. TF1, on the other hand, showed a steady-state behavior with a rapid increase to reach 300 ^{o}C within 2 min without breakingdown electrically. Therefore, it was tested repeatedly to observe its behavior under cyclic heating and cooling. After repeating the same experiments under the same conditions, the saturation temperature was found to be within the range of acceptable experimental error. Since one of the main concern of this study was related with efficiency, the efficiency calculations were done regarding electrical energy (input) converted into heat (output). According to the calculations, the efficiency of bare AISI 304 SS was calculated to be around 7.3% while thin FTO coated sample (TF1) was found as 28.6%. This result proves that, using thin FTO film as a replacement for the heating element would increase the overall efficiency dramatically.

For the humidity test, the samples (TF1-TF5) were left in a chamber that is capable of supplying 95% relative humidity atmosphere for 10 days with alternating temperature values between 20-60 ^{o}C without any interruption. After completion of the test, the samples were removed from their holders and inspected. Even though the sample TF1 showed some degradation due to edge effect, the remaining part of the sample and other samples (TF2-TF5) were not degraded or failed. Sheet resistance measurements were conducted to compare the change (less than 5%) in the resistivity values of the samples before and after humidity test. The calculations showed that there is almost

no change in their resistivity and sheet resistance values. These results clearly suggest that the FTO coatings are resistant against moist atmosphere which makes them quite suitable for applications that operate under similar environmental conditions.

In conclusion, the production of fluorine doped tin dioxide (FTO) coated AISI 304 stainless steel substrates with TiO_2 intermediate layer was successfully achieved using ultrasonic spray pyrolysis method upon optimization of the process parameters. This process was deliberately selected due to its ability to be converted into mass production with high quality. Achieving thick insulating layer delays the occurrence of breakdown phenomenon under the applied voltage. Although FTO alone breaks down electrically with 6 V, existence of TiO_2 buffer layer in between increases working voltage to 12 V, even at high temperatures around 300 ^{o}C. With the help of this, the samples were heated using electrical power around 300 ^{o}C without any problem, even with cyclic heating. In the end, the use of efficient conversion of electrical energy into heat enables us to reach desired temperatures. Besides, the overall temperature distribution can be made much more homogeneous throughout the surface by using thin film heaters that is perfectly suitable for replacement of commercial resistance heaters.

REFERENCES

[1] British Petroleum, BP Statistical Review of World Energy 2017, Br. Pet. (2017) 1–52.

[2] M. Sakr, S. Liu, A comprehensive review on applications of ohmic heating (OH), Renew. Sustain. Energy Rev. 39 (2014) 262–269.

[3] A. Aid, Comparison of Thin-film and Wire-element Heaters for Transparent Applications, Minco Inf. Leafl. (2002) 1–8.

[4] D. Malec, V. Bley, F. Talbi, F. Lalam, Contribution to the understanding of the relationship between mechanical and dielectric strengths of Alumina, J. Eur. Ceram. Soc. 30 (2010) 3117–3123.

[5] D.S. Jung, S. Bin Park, Y.C. Kang, Design of particles by spray pyrolysis and recent progress in its application, Korean J. Chem. Eng. 27 (2010) 1621–1645.

[6] A.R. Babar, S.S. Shinde, A. V. Moholkar, C.H. Bhosale, K.Y. Rajpure, Structural and optoelectronic properties of sprayed Sb:SnO_2 thin films: Effects of substrate temperature and nozzle-to-substrate distance, J. Semicond. 32 (2011) 102001.

[7] S. Yu, H. Zheng, L. Li, S. Chen, Highly conducting and transparent antimony doped tin oxide thin films: the role of sputtering power density, Ceram. Int. 43 (2017) 5654–5660.

[8] A. Purwanto, Transparent and conductive flourinated-tin oxide prepared by atmospheric deposition technique, Adv. Mater. Res. 896 (2014) 24–28.

[9] L. He, S.C. Tjong, Nanostructured transparent conductive films: Fabrication, characterization and applications, Mater. Sci. Eng. R Reports. 109 (2016) 1–101.

[10] P.S. Joshi, S.M. Jogade, P.A. Lohar, D.S. Sutrave, D.B.F. Dayanand, Antimony Doped Tin Oxide Thin Films: Co Gas Sensor, J. Nano-Electron. Phys. SumDU. 3 (2011) 956–962.

[11] Z. Banyamin, P. Kelly, G. West, J. Boardman, Electrical and Optical Properties of Fluorine Doped Tin Oxide Thin Films Prepared by Magnetron Sputtering, Coatings. 4 (2014) 732–746.

[12] S. Hwang, Y.Y. Kim, J.H. Lee, D.K. Seo, J.Y. Lee, H.K. Cho, Irregular electrical conduction types in tin oxide thin films induced by nanoscale phase separation, J. Am. Ceram. Soc. 95 (2012) 324–327.

[13] M.A. Aouaj, R. Diaz, A. Belayachi, F. Rueda, M. Abd-Lefdil, Comparative study of ITO and FTO thin films grown by spray pyrolysis, Mater. Res. Bull. 44 (2009) 1458–1461.

[14] J.H. Park, B.J. Jeon, J.K. Lee, Electrochemical characteristics of fluorine-doped tin oxide film coated on stainless steel bipolar plates, Surf. Coatings Technol. 277 (2015) 1–6.

[15] J.H. Park, D. Byun, J.K. Lee, Employment of fluorine doped zinc tin oxide ($ZnSnO_x$:F) coating layer on stainless steel 316 for a bipolar plate for PEMFC, Mater. Chem. Phys. 128 (2011) 39–43.

[16] A.R. Babar, S.S. Shinde, A. V. Moholkar, C.H. Bhosale, J.H. Kim, K.Y. Rajpure, Physical properties of sprayed antimony doped tin oxide thin films: The role of thickness, J. Semicond. 32 (2011) 053001.

[17] S. Ben Ameur, A. Barhoumi, H. Bel hadjltaief, R. Mimouni, B. Duponchel, G. Leroy, M. Amlouk, H. Guermazi, Physical investigations on undoped and Fluorine doped SnO_2 nanofilms on flexible substrate along with wettability and photocatalytic activity tests, Mater. Sci. Semicond. Process. 61 (2017) 17–26.

[18] R. Buntem, P. Kraisingdecha, W. Sadee, Fluoride and Antimony-Doped Tin Oxide Film by Spray Pyrolysis, Adv. Mater. Res. 55–57 (2008) 513–516.

[19] M. Nuño, R.J. Ball, C.R. Bowen, R. Kurchania, G.D. Sharma, Photocatalytic activity of electrophoretically deposited (EPD) TiO_2 coatings, J. Mater. Sci. 50 (2015) 4822–4835.

[20] G. Jain, R. Kumar, Electrical and optical properties of tin oxide and antimony doped tin oxide films, Opt. Mater. (Amst). 26 (2004) 27–31.

[21] A. V. Moholkar, S.M. Pawar, K.Y. Rajpure, C.H. Bhosale, J.H. Kim, Effect of fluorine doping on highly transparent conductive spray deposited nanocrystalline tin oxide thin films, Appl. Surf. Sci. 255 (2009) 9358–9364.

[22] H. Bisht, H.-T. Eun, a Mehrtens, M.. Aegerter, Comparison of spray pyrolyzed FTO, ATO and ITO coatings for flat and bent glass substrates, Thin Solid Films. 351 (1999) 109–114.

[23] C. Goebbert, R. Nonninger, M.. Aegerter, H. Schmidt, Wet chemical deposition of ATO and ITO coatings using crystalline nanoparticles redispersable in solutions, Thin Solid Films. 351 (1999) 79–84.

[24] H.P. Dang, Q.H. Luc, T. Le, V.H. Le, The Optimum Fabrication Condition of p-Type Antimony Tin Oxide Thin Films Prepared by DC Magnetron Sputtering, J. Nanomater. 2016 (2016) 24–30.

[25] S. Shanthi, C. Subramanian, P. Ramasamy, Growth and characterization of antimony doped tin oxide thin films, J. Cryst. Growth. 197 (1999) 858–864.

[26] J.K. Lee, J. Park, D. Byun, Employement of Fluorine doped Tin Oxide coated Stainless Steel Bipolar Plate for Proton Exchange Membrane Fuel Cell, Mat. Chem. and Phys. 128 (2011) 39-43.

[27] A. V. Moholkar, S.M. Pawar, K.Y. Rajpure, S.N. Almari, P.S. Patil, C.H. Bhosale, Solvent-dependent growth of sprayed FTO thin films with mat-like morphology, Sol. Energy Mater. Sol. Cells. 92 (2008) 1439–1444.

[28] A.A. Yadav, E.U. Masumdar, A. V. Moholkar, K.Y. Rajpure, C.H. Bhosale, Effect of quantity of spraying solution on the properties of spray deposited fluorine doped tin oxide thin films, Phys. B Condens. Matter. 404 (2009) 1874–1877.

[29] T.-Y. Cho, C.-W. Han, S.-G. Yoon, Transparent conducting oxide free dye sensitized solar cell using flexible stainless steel mesh, J. Alloys Compd. 578 (2013) 609–612.

[30] C. Hudaya, B.J. Jeon, J.K. Lee, High thermal performance of SnO_2:F thin transparent heaters with scattered metal nanodots, ACS Appl. Mater. Interfaces. 7 (2015) 57–61.

[31] A. Czapla, E. Kusior, M. Bucko, Optical properties of non-stoichiometric tin oxide films obtained by reactive sputtering, Thin Solid Films. 182 (1989) 15–22.

[32] S. Farhadi, Z. Roostaei-Zaniyani, Preparation and characterization of NiO nanoparticles from thermal decomposition of the $[Ni(en)_3](NO_3)_2$ complex: A facile and low-temperature route, Polyhedron. 30 (2011) 971–975.

[33] W. Zhang, S. Ding, Z. Yang, A. Liu, Y. Qian, S. Tang, S. Yang, Growth of novel nanostructured copper oxide (CuO) films on copper foil, J. Cryst. Growth. 291 (2006) 479–484.

[34] M. Batzill, U. Diebold, The surface and materials science of tin oxide, Prog. Surf. Sci. 79 (2005) 47–154.

[35] K.C. Icli, B.C. Kocaoglu, M. Ozenbas, Comparative study on deposition of fluorine-doped tin dioxide thin films by conventional and ultrasonic spray pyrolysis methods for dye-sensitized solar modules, J. Photonics Energy. 8 (2018) 015501.

[36] A. Jilani, M.S. Abdel-wahab, A.H. Hammad, Modern Technologies for Creating the Thin-film Systems and Coatings, IntechOpen (2017) 137-149.

[37] T. Koida, H. Fujiwara, M. Kondo, Hydrogen-doped In_2O_3 as high-mobility transparent conductive oxide, Japanese J. Appl. Physics, Part 2 Lett. 46 (2007) L685-687.

[38] M. Henini, Handbook of Thin-Film Deposition Processes and Techniques, Noyes, New York (2000).

[39] H. Shen, H. Zhang, L. Lu, F. Jiang, C. Yang, Preparation and properties of AZO thin films on different substrates, Prog. Nat. Sci. Mater. Int. 20 (2010) 44–48.

[40] N. Noor, I.P. Parkin, Enhanced transparent-conducting fluorine-doped tin oxide films formed by Aerosol-Assisted Chemical Vapour Deposition, J. Mater. Chem. C. 1 (2013) 984–996.

[41] T. Minami, Transparent conducting oxide semiconductors for transparent electrodes, Semicond. Sci. Technol. 20 (2005) S35-S44.

[42] D.R. Acosta, E.P. Zironi, E. Montoya, W. Estrada, About the structural, optical and electrical properties of SnO_2 films produced by spray pyrolysis from solutions with low and high contents of fluorine, Thin Solid Films. 288 (1996) 1–7.

[43] C. Falcony, Luminescent Characteristics of Tb Doped Al_2O_3 Films Deposited by Spray Pyrolysis, J. Electrochem. Soc. 139 (1992) 267–270.

[44] M. Fujimoto, T. Urano, S. Murai, Y. Nishi, Microstructure and x-ray study of preferentially oriented SnO_2 thin film prepared by pyrohydrolytic decomposition, Jpn. J. Appl. Phys. 28 (1989) 2587–2593.

[45] R.R. Chamberlin, J.S. Skarman, Chemical Spray Deposition Process fr Inorganic Films, Electrochem. Soc. (1966) 86–89.

[46] Q. Guo, G.M. Ford, W. Yang, B.C. Walker, E.A. Stach, H.W. Hillhouse, R. Agrawal, Fabrication of 7.2% Efficient CZTSSe Solar Cells Using CZTS Nanocrystals, J. Am. Chem. Soc. 132 (2010) 17384–17386.

[47] K.O. Ukoba, A.C. Eloka-Eboka, F.L. Inambao, Review of nanostructured NiO thin film deposition using the spray pyrolysis technique, Renew. Sustain. Energy Rev. 82 (2018) 2900–2915.

[48] D. Davazoglou, K. Georgouleas, Low pressure chemically vapor deposited WO_3 thin films for integrated gas sensor applications, J. Electrochem. Soc. 145 (1998) 1346–1350.

[49] P.S. Patil, L.D. Kadam, C.D. Lokhande, Preparation and characterization of spray pyrolysed cobalt oxide thin films, Thin Solid Films. 272 (1996) 29–32.

[50] C.H. Chen, A.A.J. Buysman, E.M. Kelder, J. Schoonman, Fabrication of $LiCoO_2$ thin film cathodes for rechargeable lithium battery by electrostatic spray pyrolysis, Solid State Ionics. 80 (1995) 1–4.

[51] H.D.B. S. Saha, U. Pal, A.K. Chaudhuri, V.V. Rao, Optical properties of CdTe thin films, Appl. Mater. Sci. 114 (1989) 721–729.

[52] O.N.S. H.K. Singh, A.K. Saxena, The synthesis of HTSC films through spray pyrolysis and an evaluation of the influence of silver on the critical current density, Supercond. Sci. Technol. 8 (1995) 448–454.

[53] D. Kim, J. Park, J.H. Kim, Y.C. Kang, H.S. Kim, Thermoelectric properties of solution-processed antimony-doped tin oxide thin films, Thin Solid Films. 646 (2018) 92–97.

[54] C. Goebbert, H. Bisht, N. Al-Dahoudi, R. Nonninger, M.A. Aegerter, H. Schmidt, Wet chemical deposition of crystalline, redispersable ATO and ITO nanoparticles, J. Sol-Gel Sci. Technol. 19 (2000) 201–204.

[55] S.J. Kang, Y.H. Joung, Influence of substrate temperature on the optical and piezoelectric properties of ZnO thin films deposited by rf magnetron sputtering, Appl. Surf. Sci. 253 (2007) 7330–7335.

[56] S. Yu, H. Zheng, L. Li, S. Chen, Highly conducting and transparent antimony doped tin oxide thin films: the role of sputtering power density, Ceram. Int. 43 (2017) 5654–5660.

[57] L.W. Martin, Y.H. Chu, R. Ramesh, Advances in the growth and characterization of magnetic, ferroelectric, and multiferroic oxide thin films, Mater. Sci. Eng. R Reports. 68 (2010) 89–133.

[58] C. Viespe, I. Nicolae, C. Sima, C. Grigoriu, R. Medianu, ITO thin films deposited by advanced pulsed laser deposition, Thin Solid Films. 515 (2007)

[59] C. Vahlas, B. Caussat, P. Serp, G.N. Angelopoulos, Principles and applications of CVD powder technology, Mater. Sci. Eng. R Reports. 53 (2006) 1–72.

[60] Y.H. Chen, H.Y. Fang, C.M. Yeh, Raman scattering and electrical characterizations studies of hydrogenated amorphous silicon-germanium alloys prepared by 40 MHz plasma-enhanced CVD, J. Non. Cryst. Solids. 357 (2011) 1–3.

[61] J.M. Lamarre, P. Marcoux, M. Perrault, R.C. Abbott, J.G. Legoux, Performance analysis and modeling of thermally sprayed resistive heaters, J. Therm. Spray Technol. 22 (2013) 947–953.

[62] V.L. Gurevich, M.I. Muradov, Release of the Joule heat upon passage of the electric current in nanostructures, Phys. Solid State. 54 (2012) 663–681.

[63] F. El-Kabbany, W. Badawy, N.H. Tahr, E.H. El-Khwas, Joule heating and breakdown effects in KNO_3 thin layers, J. Mater. Sci. 23 (1988) 583–587.

[64] M. Zell, J.G. Lyng, D.J. Morgan, D.A. Cronin, Development of rapid response thermocouple probes for use in a batch ohmic heating system, J. Food Eng. 93 (2009) 344–347.

[65] G.A. Vorob'ev, N.S. Nesmelov, Electric breakdown in solid dielectrics, Sov. Phys. J. 22 (1979) 70–80.

[66] N. Gonzalez, Can Lightning Strike the Same Place Twice, (n.d.). https://www.britannica.com/story/can-lightning-strike-the-same-place-twice.

[67] R. Dorey, Ceramic Thick Films for MEMS and Microdevices, Elsevier (2011) 85-112.

[68] L. Haddour, N. Mesrati, D. Goeuriot, D. Tréheux, Relationships between microstructure, mechanical and dielectric properties of different alumina materials, J. Eur. Ceram. Soc. 29 (2009) 2747–2756.

[69] C. Neusel, H. Jelitto, D. Schmidt, R. Janssen, F. Felten, G.A. Schneider, Thickness-dependence of the breakdown strength: Analysis of the dielectric and mechanical failure, J. Eur. Ceram. Soc. 35 (2015) 113–123.

[70] C. Neusel, G.A. Schneider, Size-dependence of the dielectric breakdown strength from nano- to millimeter scale, J. Mech. Phys. Solids. 63 (2014) 201–213.

[71] E.K. Beauchamp, Pulse Electrical Strength of MgO, J. Am. Ceram. Soc. 54 (1971) 484–487.

[72] M. Nafría, J. Suñé, X. Aymerich, Breakdown of thin gate silicon dioxide films, Microelectron. Reliab. 36 (1996) 871–905.

[73] S. Al-Khateeb, D. Pavlopoulos, T.W. Button, J.S. Abell, Spray pyrolysis of MgO templates on 321-austenitic stainless steel substrates for $YBa_2Cu_3O_7$ deposition by PLD, J. Supercond. Nov. Magn. 26 (2013) 273–280.

[74] F.C. Nascimento, C.E. Foerster, S.L.R. da Silva, C.M. Lepienski, C.J. de M. Siqueira, C. Alves Junior, A comparative study of mechanical and tribological properties of AISI-304 and AISI-316 submitted to glow discharge nitriding, Mater. Res. 12 (2009) 173–180.

[75] Agilent Technologies, Laser and Optics User's Manual, USA (2002) Chapter 17.

[76] J.W. Anthony, R. a. Bideaux, K.W. Bladh, M.C. Nichols, Mineral Data Publishing, version 1 (2001-2005).

[77] L. Iyengar, K.V.K. Rao, S.V.N. Naidu, Thermal Expansion of Rutile and Anatase, J. Am. Ceram. Soc. 53 (1969) 124.

[78] S.A. Yousif, J.M. Abass, Structural, Morphological and Optical Characterization of SnO_2:F thin films prepared by Chemical spray Pyrolysis, Int. Lett. Chem. Phys. Astron. 13 (2013) 90–102.

[79] M. Fukawa, K. Sato, T. Tsukamoto, K. Adachi, H. Nishimura, Development of tempered-glass substrates with TCO films for a-Si solar cells, Sol. Energy Mater. Sol. Cells. 49 (1997) 107–112.

[80] Silica – Silicon Dioxide (SiO_2), AZO Materials (2001) https://www.azom.com/article.aspx?ArticleID=1114

[81] Alumina - Aluminium Oxide - Al_2O_3 - A Refractory Ceramic Oxide, AZO Materials (2001) https://www.azom.com/article.aspx?ArticleID=52

[82] Magnesia - Magnesium Oxide (MgO) Properties & Applications, AZO Materials (2001) https://www.azom.com/article.aspx?ArticleID=54

[83] T. Jäger, B. Bissig, M. Döbeli, A.N. Tiwari, Y.E. Romanyuk, Thin films of SnO_2:F by reactive magnetron sputtering with rapid thermal post-annealing, Thin Solid Films. 553 (2014) 21–25.

[84] S.F. Tseng, W.T. Hsiao, D. Chiang, K.C. Huang, C.P. Chou, Mechanical and optoelectric properties of post-annealed fluorine-doped tin oxide films by ultraviolet laser irradiation, Appl. Surf. Sci. 257 (2011) 7204–7209.

[85] MIL-STD-810G, Department Of Defense Test Method Standard: Environmental Engineering Considerations and Laboratory Tests, American Department of Defense (2014).